A Matrix-Dependent Transfer Multigrid Method for Strongly Variable Viscosity Infinite Prandtl Number Thermal Convection

Woo-Sun Yang
Institute of Geophysics and Planetary Physics, University of California, Los Angeles;
Institute of Geophysics and Planetary Physics, MS C305
Los Alamos National Laboratory, Los Alamos, NM 85745

John R. Baumgardner
Theoretical Division, MS B216,
Los Alamos National Laboratory, Los Alamos, NM 87545

Submitted to *Geophysical and Astrophysical Fluid Dynamics*

January 27, 1999

Abstract

We apply a 2-D Cartesian finite element treatment to investigate infinite Prandtl number thermal convection with temperature, strain rate and yield stress dependent rheology. To handle the strong viscosity variations that arise from nonlinear rheology we rely on a multigrid solver for the momentum equation based on a matrix-dependent intergrid transfer and Galerkin coarse grid approximation. We observe that the matrix-dependent transfer algorithm provides an extremely robust and efficient means for solving such convection problems when the gradients in viscosity are large. The algorithm is explained in detail in this paper.

When this method is applied to problems with strain rate and yield stress dependent rheology, we obtain time dependent solutions characterized by episodic avalanching of cold material from the upper boundary layer to the bottom of the convecting domain. The intensity of this behavior depends on the yield stress and on the threshold strain rate for power-law behavior in the deformation law. The regions most strongly affected by the yield stress are thickened portions of the cold upper boundary layer which can suddenly become unstable and form downgoing diapirs. This suggests that the finite yield properties of silicate rocks may play a very important role in planetary mantle dynamics. The extreme weakening of the cold upper lid induces episodic catastrophic overturns in which the vertical mass flux increases by orders of magnitude. This behavior occurs both for strongly strain rate dependent rheology and for rheology restricted by a finite yield stress.

Keywords: mantle convection, rheology, yield stress, multigrid, matrix-dependent transfer

1 Introduction

Plate tectonics is the surface manifestation of convection in the deep interior of Earth's mantle. Fluid mechanical simulations of the plate/mantle system have proven to be very difficult, owing mainly to the extreme rheological variations that mantle rocks undergo with changes in temperature, pressure, and strain rate. Another fundamental limitation on mantle convection studies has been the difficulty in simulating fracture, or pronounced yielding, at plate boundaries. Here we present a numerical methodology for fluid dynamic modeling of mantle convection with extreme variations in effective viscosity, thus allowing treatment of diverse rheological laws that may apply to mantle convection and give rise to plate-like behavior in the Earth and other terrestrial planets. In particular, we treat both Newtonian and non-Newtonian creep, strongly temperature-dependent viscosity, and visco-plastic or finite yield stress rheologies. Relevant combinations of these rheologies result in rather behavior, including strong episodicity in flow and heat transport, which have not been observed before in numerical simulations.

Earth materials under stress exhibit slow, thermally-activated creep deformation via rearrangement and adjustment of lattice defects such as vacancies and dislocations within mineral grains as well as displacements along grain boundaries. The rheological relationship between creep strain rate and stress can be expressed as an effective viscosity for the solid. For the Earth's silicate materials, creep appears to be governed by complicated systematics. Silicate rheology has been observed to be dependent on temperature, pressure, strain-rate and mineral grain size, etc. (e.g., Weertman, 1970; Weertman and Weertman, 1975; Stocker and Ashby, 1973; Ranalli, 1991). Moreover, depending on temperature and pressure conditions, deformation behavior can be either insensitive to or strongly dependent on the strain-rate. Strain-rate dependence implies stress is a nonlinear function of strain rate, i.e., that rheology is non-Newtonian. Seismic observations as well as geodynamic modelling suggest there may be rheological layering in the Earth's mantle where non-Newtonian rheology is dominant in the upper few hundred km and Newtonian

rheology characterizes deformation at greater depths (Karato and Wu, 1993). There is strong evidence that non-Newtonian deformation plays an important role in the Earth's upper mantle and helps mobilize the lithosphere and make plate tectonics possible. Recent numerical studies indicate that a finite yield stress may play the crucial role in mobilizing the cold lithosphere which otherwise would be immobile due to its low temperature (Moresi and Solomatov, 1998; Trompert and Hansen, 1998). To fully investigate such complex rheological behavior in a numerical model it is essential to be able to accommodate extreme gradients in rheological strength in a robust way.

We formulate the mantle convection problem with such nonlinear variable viscosity using the finite element method and apply a special multigrid approach to solve the resulting matrix equation. The standard multigrid approach that utilizes linear interpolation for intergrid transfers is inadequate for such problems because of its poor convergence properties when operator coefficients are strongly variable or discontinuous. Since Alcouffe, Brandt, Dendy and Painter (1981) first devised an interpolation scheme in which the interpolation weights in prolongation and restriction operations depend on the differential operator values, many workers have reported striking success with their matrix-dependent transfer approach for a wide spectrum of applications (Kettler, 1982; de Zeeuw, 1990; Reusken, 1993; Reusken, 1994; Wagner, 1994). We apply this matrix-dependent transfer idea to our problem of high Prandtl number variable viscosity thermal convection. The approach presented here, however, differs from the cases reported above in that those formulations involve scalar differential operators and scalar unknowns while our formulation involves a tensor differential operator and a vector unknown. Our implementation of the idea, therefore, inevitably requires a measure of simplification, but we find that the matrix-dependent transfer strategy provides a robust and efficient way to solve the vector problem with strongly variable operator coefficients.

2 Numerical Formulation

The solid state creep rheology of the Earth's mantle allows us to treat the mantle's silicate material as a viscous fluid on geologic time scales ($> 10^6$ years). The viscosity of this material is on the order of 10^{21} Pa sec which implies a Prandtl number on the order of 10^{24}. This fact allows us to ignore the inertial terms in the momentum equation (Turcotte, Torrance and Hsui, 1973). Assuming anelasticity (e.g., Jarvis and McKenzie, 1980; Glatzmaier, 1988) and the Boussinesq equation of state, thermal convection in the 2-D rectangular mantle can then be described by the equations for the conservation of mass, momentum and energy (e.g., Baumgardner, 1983; Baumgardner, 1985):

$$\frac{\partial(\rho u_m)}{\partial x_m} = 0 \tag{1}$$

$$\frac{\partial \tau_{lm}}{\partial x_m} - \frac{\partial p}{\partial x_l} + \rho_0 g \alpha (T - T_0)\, \delta_{l2} = 0 \qquad (l = 1, 2) \tag{2}$$

$$\frac{\partial T}{\partial t} = -\frac{\partial (T u_l)}{\partial x_l} - (\gamma - 1) T \frac{\partial u_l}{\partial x_l} + \frac{1}{\rho c_V}\left[\tau_{lm}\frac{\partial u_m}{\partial x_l} + \frac{\partial}{\partial x_l}\left(k\frac{\partial T}{\partial x_l}\right) + \rho H\right] \tag{3}$$

where $\mathbf{u}$, τ, p, ρ, ρ_0, g, α, T, T_0, γ, c_V, k and H are the velocity, deviatoric stress, dynamic pressure, density, reference density, gravitational acceleration (which is approximately constant through the Earth's mantle), thermal expansion coefficient, temperature, reference temperature, Grueneisen parameter, specific heat at constant volume, thermal conductivity and radiogenic heat generation rate per unit mass, respectively. It is assumed that $y \equiv x_2$ increases in the upward direction. The deviatoric stress can be related to velocity by a constitutive relation

$$\tau_{lm} = \mu\left(\frac{\partial u_l}{\partial x_m} + \frac{\partial u_m}{\partial x_l}\right) + (K - \mu)\, \delta_{lm}\frac{\partial u_k}{\partial x_k} \tag{4}$$

where μ is effective dynamic viscosity, K is the bulk viscosity and δ_{lm} is the Kronecker delta. For 3-D cases $(K - \mu)$ is replaced with $(K - \frac{2}{3}\mu)$. As indicated in the previous section, the effective viscosity of mantle materials is dependent on many physical quantities including temperature, pressure, strain-rate, mineral grain size.

We obtain a solution to this system by first solving simultaneously (1), (2) and (4) for velocity and pressure, and then solving (3) for temperature. The physical domain is a rectangle defined by $0 < x < w$ and $0 < y < h$ (h is set to 2890 km, the thickness of the Earth's mantle) which is discretized into an $(n_1+1)\times(n_2+1)$ rectangular mesh of points as shown in FIGURE 1. The velocity field is represented in discrete form by its nodal values u_{il} $(i = 1, 2, \ldots, (n_1+1)(n_2+1);\ l = 1, 2)$ and almost all the other physical variables are represented in terms of their values at cell centers (for example, temperature is represented by T_I, the value in cell I $(I = 1, 2, \ldots, n_1 n_2)$. To impose boundary conditions we add two ghost layers of cells and nodes beyond the real physical domain on each of its four sides. The appropriate boundary conditions at the top and bottom boundaries are zero normal velocity and zero shear stress:

FIGURE 1

$$u_y = 0 \quad \text{and} \quad \tau_{xy} = \tau_{yx} = 0 \quad \text{at} \quad y = 0, h \tag{5}$$

which can be imposed by specifying ghost node velocities according to the reflective boundary condition at both boundaries:

$$\begin{aligned} u_x(y) &= u_x(-y), & u_y(y) &= -u_y(-y), \\ u_x(h+y) &= u_x(h-y), & u_y(h+y) &= -u_y(h-y). \end{aligned} \tag{6}$$

The side boundary conditions are either reflective

$$u_x = 0 \quad \text{and} \quad \tau_{xy} = \tau_{yx} = 0 \quad \text{at} \quad x = 0, w \tag{7}$$

or periodic

$$u_x(x+w) = u_x(x), \qquad u_y(x+w) = u_y(x) \tag{8}$$

which can also be easily imposed applying proper velocity values at the ghost nodes. By adding these ghost nodes and specifying ghost node velocities, we are implicitly assuming

that the infinite 2-D plane, comprised of the real physical domain plus imaginary domains generated by infinitely repeating reflective or periodic boundary conditions in all four directions, represents the physical domain.

We apply the finite element method to discretize (1) and (2) and adopt piecewise linear shape functions $\{N_i\}$ for velocity and piecewise constant shape functions $\{M_I\}$ for pressure and temperature for rectangular finite element cells. This approach defines a 9-point stencil as displayed in FIGURE 1. The finite element formulation prescribes

$$\int M_I \frac{\partial(\rho u_m)}{\partial x_m}\, da = 0 \tag{9}$$

and

$$\int N_i \left[\frac{\partial \tau_{lm}}{\partial x_m} - \frac{\partial p}{\partial x_l} + \rho_0 g \alpha (T - T_0)\, \delta_{l2}\right] da = 0 \tag{10}$$

for $I = 1, 2, \ldots, n_1 n_2$, $i = 1, 2, \ldots, (n_1+1)(n_2+1)$, and $l = 1, 2$. Here, $\int (\cdot)\, da$ means an area integration over the entire 2-D plane. Since an integration is made over the infinite 2-D plane, any boundary integral containing a shape function in its integrand (which usually arises upon integrating by parts) vanishes. Letting $\mathbf{u}$ and p be column vectors for $\{u_{il}\}$ and $\{p_I\}$, respectively, the equations can be written as two sets of matrix equations:

$$G^T \mathbf{u} = 0 \tag{11}$$

$$A\mathbf{u} - Gp = \mathbf{f} \tag{12}$$

where G is a $(2(n_1+1)(n_2+1)) \times (n_1 n_2)$ matrix for a gradient operation:

$$G_{il,I} = -\int M_I \frac{\partial N_i}{\partial x_l}\, da = -\int_{\text{cell } I} \frac{\partial N_i}{\partial x_l}\, da, \tag{13}$$

A is a $(2(n_1+1)(n_2+1)) \times (2(n_1+1)(n_2+1))$ tensor operator (a tensor with respect to

indices l and m; i and j are node indices):

$$A_{iljm} = -\delta_{lm} \int \mu \frac{\partial N_i}{\partial x_k} \frac{\partial N_j}{\partial x_k}\, da - \int \mu \frac{\partial N_i}{\partial x_m} \frac{\partial N_j}{\partial x_l}\, da - \int (K - \mu) \frac{\partial N_i}{\partial x_l} \frac{\partial N_j}{\partial x_m}\, da \tag{14}$$

which is negative definite for any viscosity field (Yang, 1997), and $\mathbf{f}$ is a $(2(n_1+1)(n_2+1))\times 1$ column vector:

$$f_{il} = -\delta_{l2} \int N_i\, \rho_0 g \alpha (T - T_0)\, da. \tag{15}$$

G and A can be readily computed. A_{iljm} for $i \neq j$ is computed from the expression

$$A_{iljm} \approx -\overline{\mu}_{ij} \left[\delta_{lm} \int \frac{\partial N_i}{\partial x_k} \frac{\partial N_j}{\partial x_k}\, da + \int \frac{\partial N_i}{\partial x_m} \frac{\partial N_j}{\partial x_l}\, da + \left(\frac{\overline{K}_{ij}}{\overline{\mu}_{ij}} - 1 \right) \int \frac{\partial N_i}{\partial x_l} \frac{\partial N_j}{\partial x_m}\, da \right] \tag{16}$$

(a summation on k only)

where $\overline{\mu}_{ij}$ and $\overline{K}_{ij}$ are, respectively, the average effective viscosity and bulk viscosity for the cells containing both nodes i and j. Since by (4) constant velocity field generates zero stress, the A operator should produce a null vector when operated on any arbitrary constant velocity field (see, Patankar, 1980, p.38). This requirement can be met by specifying

$$A_{ilim} = -\sum_{j \neq i} A_{iljm} \qquad \text{(no sum on } i\text{)} \tag{17}$$

where the summation is over all nodes except node i of the stencil centered at node i. The operator values at ghost nodes can be specified in accordance with the boundary conditions. If the boundary has a reflective boundary condition, the operators connecting ghost nodes i' and j' are related to those connecting their respective mirror nodes, real nodes i and j, by

$$\begin{aligned} A_{i'1j'1} &= A_{i1j1}, \quad & A_{i'1j'2} &= -A_{i1j2} \\ A_{i'2j'1} &= -A_{i2j1}, \quad & A_{i'2j'2} &= A_{i2j2}. \end{aligned} \tag{18}$$

If a boundary has a periodic boundary condition, then the following relations hold

$$\begin{aligned} A_{i''1j''1} &= A_{i1j1}, \quad A_{i''1j'2} = A_{i1j2} \\ A_{i''2j''1} &= A_{i2j1}, \quad A_{i''2j'2} = A_{i2j2}. \end{aligned} \tag{19}$$

when nodes i'' and j'' are displaced by $\pm w$ in the x-direction from i and j, respectively.

To solve (11) and (12) for $\mathbf{u}$ and p, we use the conjugate gradient algorithm outlined by Ramage and Walthan (1992) which Yang (1997) finds satisfactory in his calculations of thermal convection in a thick spherical shell. The pseudo code is presented in TABLE I. TABLE I

To solve the energy equation a finite volume treatment is applied to the square cells of the domain. The convection term is treated in a similar fashion as the upwind scheme. The finite volume term for cell (i_1, i_2) is given by

$$\int_{\text{cell}} \frac{\partial (T u_l)}{\partial x_l}\, da = \left(T u_x \Big|_E - T u_x \Big|_W \right) \Delta y + \left(T u_y \Big|_N - T u_y \Big|_S \right) \Delta x \tag{20}$$

where $\Delta x = \Delta y$ is grid spacing $w/n_1 = h/n_2$ and E, W, S and N refer to the east, west, south and north faces of the cell. Each term on the right hand side of the equation can be evaluated in the following manner:

$$T u_x \Big|_E = \begin{cases} \left[T(i_1 - 1, i_2) + \left\langle \dfrac{\partial T}{\partial x} \right\rangle \dfrac{\Delta x}{2} \right] u_x \Big|_E, & u_x \Big|_E > 0 \\ \left[T(i_1, i_2) - \left\langle \dfrac{\partial T}{\partial x} \right\rangle \dfrac{\Delta x}{2} \right] u_x \Big|_E, & u_x \Big|_E < 0 \end{cases} \tag{21}$$

etc., where $\langle \partial T / \partial x \rangle$ is the gradient term modified with monotonicity condition of the local data. Without the monotonicity condition the finite volume gradient approximations tend to introduce severe overshoots or undershoots in the vicinity of steep gradients. The gradient term is evaluated using the van Leer's limiting method (van Leer, 1979) as

$$\begin{aligned} \left\langle \frac{\partial T}{\partial x} \right\rangle &= \alpha \frac{\partial T}{\partial x} \\ \left\langle \frac{\partial T}{\partial y} \right\rangle &= \alpha \frac{\partial T}{\partial y} \end{aligned} \tag{22}$$

where α is a limiting coefficient between 0 and 1 given by

$$\alpha = \min(1, \alpha_1, \alpha_2). \tag{23}$$

α_1 and α_2 are auxiliary coefficients defined as

$$\begin{aligned} \alpha_1 &= \max\left\{0, \left[T'_{\max} - T(i_1, i_2)\right] / \left[T_{\max} - T(i_1, i_2)\right]\right\} \\ \alpha_2 &= \max\left\{0, \left[T'_{\min} - T(i_1, i_2)\right] / \left[T_{\min} - T(i_1, i_2)\right]\right\} \end{aligned} \tag{24}$$

where $T'_{\max}$ and $T'_{\min}$ are the maximum and minumum values of T among the eight neighboring cells and $T_{\max}$ and $T_{\min}$ are the maximum and minimum values of the values at the four corners of the cell given by

$$T(i_1, i_2) \pm \frac{\partial T}{\partial x}\frac{\Delta x}{2} \pm \frac{\partial T}{\partial y}\frac{\Delta y}{2}. \tag{25}$$

A fully explicit time integration is adopted with the maximum Courant number limited to 0.25. Because the equations for momentum and mass conservation and the equation for energy conservation are solved in succession and nonlinearity (i.e., dependence of viscosity on temperature and strain rate) becomes important in variable viscosity cases, an iterative scheme is used to find a convergent solution set $(\mathbf{u}, p, T)$ for each time step which satisfy simultaneously the conservation equations of mass, momentum and energy. That is, when a temperature solution is obtained, temperature and velocity field values are used to recompute viscosity and then a new velocity field. This velocity field is used to recompute a new temperature field. This procedure is repeated until difference in velocity l_2-norm of successive iterations becomes sufficiently small. The outermost loop in TABLE I is intended for this iteration. When flow is fully developed, in general only one to five iterations are needed to reach a convergent solution.

3 Matrix-Dependent Transfer Multigrid Method

The conjugate gradient algorithm listed in TABLE I requires that a matrix equation of the type

$$A\mathbf{u} = \mathbf{b} \tag{26}$$

be solved for $\mathbf{u}$ before the conjugate loop with $\mathbf{b} = \mathbf{f} + Gp_0$ as well as inside the loop with $\mathbf{b} = Gs_i$. This is done with the matrix-dependent transfer multigrid method with the Galerkin coarse grid approximation. FIGURE 2 shows two grid systems superimposed on each other. The nodes with dots are the coarse grid nodes. As indicated above, a 9-point stencil is adopted for this grid system. Real (as opposed to ghost) fine grid nodes (grid level k) can be indexed with (i_1, i_2) for $i_1 = 0, 1, \ldots, n_1^k$ and $i_2 = 0, 1, \ldots, n_2^k$ and real coarse grid nodes (grid level $k-1$) can be indexed with (I_1, I_2) for $I_1 = 0, 1, \ldots, n_1^{k-1}$ and $I_2 = 0, 1, \ldots, n_2^{k-1}$. Here superscripts denote the grid level. Note that the area defined by the two ghost layers of the fine grid around the real domain (that is, the rectangular strip) is the same as the area defined by the just one ghost layer of the coarse grid around the real domain. FIGURE 2

The prolongation operator, represented by a $(2(n_1^k+1)(n_2^k+1)) \times (2(n_1^{k-1}+1)(n_2^{k-1}+1))$ $P^{k,k-1}$ matrix, is used to transfer the information at the $(k-1)$-th level to the k-th level as in

$$\mathbf{z}^k = P^{k,k-1}\mathbf{z}^{k-1}. \tag{27}$$

To understand how the prolongation operator is formulated it is helpful to note there are three classes of fine grid nodes distinguished in terms of their location relative to the coarse grid nodes. Suppose that the lower left node in FIGURE 3 has the fine grid (level k) index (i_1, i_2) and the coarse grid (level $k-1$) (I_1, I_2). The fine grid node at (i_1+1, i_2) has two coarse grid nodes in its stencil in the east and west positions, and the one at (i_1, i_2+1) FIGURE 3

has two coarse grid nodes in the north and south positions, and the one at (i_1+1, i_2+1) has four coarse grid nodes in the four corners.

For the fine grid node at (i_1+1, i_2) of grid level k, we have the following 36-component A operator

$$\begin{bmatrix} A^k_{NW} & A^k_N & A^k_{NE} \\ A^k_W & A^k_C & A^k_E \\ A^k_{SW} & A^k_S & A^k_{SE} \end{bmatrix} \tag{28}$$

where $A^k_{NW}, A^k_N, A^k_{NE}$, etc are 2×2 tensor matrices for the fine grid node at (i_1+1, i_2). To see qualitatively how the two coarse grid node values are weighed in the context of a physical equation, we form a 3-point star

$$\begin{bmatrix} 0 & 0 & 0 \\ a_W & a_C & a_E \\ 0 & 0 & 0 \end{bmatrix} \tag{29}$$

where

$$a_E = \text{Trace}(A^k_{NE}) + \text{Trace}(A^k_E) + \text{Trace}(A^k_{SE}) \tag{30}$$

$$a_C = \text{Trace}(A^k_N) + \text{Trace}(A^k_C) + \text{Trace}(A^k_S) \tag{31}$$

$$a_W = \text{Trace}(A^k_{NW}) + \text{Trace}(A^k_W) + \text{Trace}(A^k_{SW}). \tag{32}$$

From this we can deduce a 2×2 prolongation operator component $P^{k,k-1}_{(i_1+1,i_2),(I_1+1,I_2)}$ of $P^{k,k-1}$ relating $\mathbf{z}^k$ at (i_1+1, i_2) to $\mathbf{z}^{k-1}$ at (I_1+1, I_2) and another operator component $P^{k,k-1}_{(i_1+1,i_2),(I_1,I_2)}$ relating $\mathbf{z}^k$ at (i_1+1, i_2) to $\mathbf{z}^{k-1}$ at (I_1, I_2):

$$P^{k,k-1}_{(i_1+1,i_2),(I_1+1,I_2)} = -\frac{a_E}{a_C}\, I_2 = \frac{a_E}{a_E + a_W}\, I_2 \tag{33}$$

$$P^{k,k-1}_{(i_1+1,i_2),(I_1,I_2)} = -\frac{a_W}{a_C}\, I_2 = \frac{a_W}{a_E + a_W}\, I_2 \tag{34}$$

where $a_C = -(a_E + a_W)$ holds because of (17), and I_2 is the 2×2 identity matrix.

Because of the form of the prolongation operators in the above equations, each Cartesian component of the fine grid field is determined in a uniform manner when performing a prolongation operation. In this case the weighting factors are intended to reflect the overall heterogeneity in physical properties around the node in question rather than the fine details on which important information might be already obscured due to lumping. Although we choose a_E, a_C, a_W, etc. to be scalars instead of 2×2 matrices and for simplicity use an identity matrix in (33) and (34), these are probably appropriate choices. Such reasoning also justifies the use of the trace, which is the simplest of the invariants of a tensor of rank two.

For the fine grid node at $(i_1, i_2 + 1)$ of FIGURE 3, we can create a 3-point star in a similar fashion from $B^k_{NW}, B^k_N, B^k_{NE}$, etc., which represents the 2×2 matrices at the fine node. The following interpolation weights can be obtained:

$$P^{k,k-1}_{(i_1,i_2+1),(I_1,I_2+1)} = -\frac{b_N}{b_C} I_2 = \frac{b_N}{b_N + b_S} I_2 \tag{35}$$

$$P^{k,k-1}_{(i_1,i_2+1),(I_1,I_2)} = -\frac{b_S}{b_C} I_2 = \frac{b_S}{b_N + b_S} I_2 \tag{36}$$

where

$$b_N = \text{Trace}(B^k_{NW}) + \text{Trace}(B^k_N) + \text{Trace}(B^k_{NE}) \tag{37}$$

$$b_C = \text{Trace}(B^k_W) + \text{Trace}(B^k_C) + \text{Trace}(B^k_E) \tag{38}$$

$$b_S = \text{Trace}(B^k_{SW}) + \text{Trace}(B^k_S) + \text{Trace}(B^k_{SE}). \tag{39}$$

For the fine grid node at $(i_1 + 1, i_2 + 1)$ of FIGURE 3, we form a 5-point star:

$$\begin{bmatrix} c_{NW} & 0 & c_{NE} \\ 0 & c_C & 0 \\ c_{SW} & 0 & c_{SE} \end{bmatrix} \tag{40}$$

and build the following interpolation weights

$$P^{k,k-1}_{(i_1+1,i_2+1),(I_1,I_2)} = -\frac{c_{SW}}{c_C}\, I_2 = \frac{c_{SW}}{c_{SW}+c_{SE}+c_{NW}+c_{NE}}\, I_2 \tag{41}$$

$$P^{k,k-1}_{(i_1+1,i_2+1),(I_1+1,I_2)} = -\frac{c_{SE}}{c_C}\, I_2 = \frac{c_{SE}}{c_{SW}+c_{SE}+c_{NW}+c_{NE}}\, I_2 \tag{42}$$

$$P^{k,k-1}_{(i_1+1,i_2+1),(I_1,I_2+1)} = -\frac{c_{NW}}{c_C}\, I_2 = \frac{c_{NW}}{c_{SW}+c_{SE}+c_{NW}+c_{NE}}\, I_2 \tag{43}$$

$$P^{k,k-1}_{(i_1+1,i_2+1),(I_1+1,I_2+1)} = -\frac{c_{NE}}{c_C}\, I_2 = \frac{c_{NE}}{c_{SW}+c_{SE}+c_{NW}+c_{NE}}\, I_2 \tag{44}$$

where

$$c_C = \mathrm{Trace}(C^k_C) \tag{45}$$

$$c_{SW} = \mathrm{Trace}(C^k_{SW}) + \frac{\mathrm{Trace}(C^k_S)\,\mathrm{Trace}(A^k_W)}{\mathrm{Trace}(A^k_E)+\mathrm{Trace}(A^k_W)} + \frac{\mathrm{Trace}(C^k_W)\,\mathrm{Trace}(B^k_S)}{\mathrm{Trace}(B^k_N)+\mathrm{Trace}(B^k_S)} \tag{46}$$

$$c_{SE} = \mathrm{Trace}(C^k_{SE}) + \frac{\mathrm{Trace}(C^k_S)\,\mathrm{Trace}(A^k_E)}{\mathrm{Trace}(A^k_E)+\mathrm{Trace}(A^k_W)} + \frac{\mathrm{Trace}(C^k_E)\,\mathrm{Trace}(D^k_S)}{\mathrm{Trace}(D^k_N)+\mathrm{Trace}(D^k_S)} \tag{47}$$

$$c_{NW} = \mathrm{Trace}(C^k_{NW}) + \frac{\mathrm{Trace}(C^k_N)\,\mathrm{Trace}(E^k_W)}{\mathrm{Trace}(E^k_E)+\mathrm{Trace}(E^k_W)} + \frac{\mathrm{Trace}(C^k_W)\,\mathrm{Trace}(B^k_N)}{\mathrm{Trace}(B^k_N)+\mathrm{Trace}(B^k_S)} \tag{48}$$

$$c_{NE} = \mathrm{Trace}(C^k_{NE}) + \frac{\mathrm{Trace}(C^k_N)\,\mathrm{Trace}(E^k_E)}{\mathrm{Trace}(E^k_E)+\mathrm{Trace}(E^k_W)} + \frac{\mathrm{Trace}(C^k_E)\,\mathrm{Trace}(D^k_N)}{\mathrm{Trace}(D^k_N)+\mathrm{Trace}(D^k_S)}. \tag{49}$$

$C^k_{NW}, C^k_N, C^k_{NE}$, etc. are the operators at (i_1+1, i_2+1), D^k_N and D^k_S are the operators at (i_1+2, i_2+1), and E^k_E and E^k_W are the operators at (i_1+1, i_2+2).

The elements of the prolongation operator whose coarse grid and fine grid indices correspond to the same physical node are set to 1:

$$P^{k,k-1}_{(i_1,i_2),(I_1,I_2)} = 1 \tag{50}$$

$$P^{k,k-1}_{(i_1+2,i_2),(I_1+1,I_2)} = 1, \quad \text{etc.} \tag{51}$$

The restriction operator, $R^{k-1,k}$, is used to construct field at the $(k-1)$-th level from one at the k-th level as in

$$\mathbf{r}^{k-1} = R^{k-1,k}\mathbf{r}^k. \tag{52}$$

The operator can be determined directly from the prolongation operator with the so called canonical choice (Hackbusch, 1982):

$$R^{k-1,k} = \left(P^{k,k-1}\right)^T. \tag{53}$$

Coarse grid operator is assembled, following the Galerkin coarse grid approximation, as

$$A^{k-1} = R^{k-1,k} A^k P^{k,k-1}. \tag{54}$$

The prolongation operator values for ghost nodes are needed to construct correct coarse grid operators at boundary nodes. The values at ghost nodes can be specified in such a way that the resulting coarse grid operator from (54) retains the symmetries dictated by the boundary conditions, i.e., (18) and (19). This requires that

$$P^{k,k-1}_{(i_1',i_2'),(I_1',I_2')} = P^{k,k-1}_{(i_1,i_2),(I_1,I_2)}. \tag{55}$$

For the reflective boundary conditions, (i_1', i_2') and (I_1', I_2') are the mirror nodes of real nodes (i_1, i_2) and (I_1, I_2), respectively and for the periodic conditions $i_1' = i_1 + n_1^k$, $i_2' = i_2$, $I_1' = I_1 + n_1^{k-1}$ and $I_2' = I_2$.

The lumping strategy presented above is similar to the procedure adopted by Reusken (1994) and Wagner (1994) for scalar field problems in which they ultimately realize the Schur complement multigrid method. The prolongation operators defined there are basically the same as $P^{k,k-1}$ here. Our approach, however, is not to follow the Schur complement approach but rather to derive interpolation weights from the fine grid operator itself and to use these in assembling the coarse grid operator at the $(k-1)$-th level. This approach provides an interesting benefit. It can be shown that the interpolation scheme expressed by the matrix $P^{k,k-1}$, reduces to the simple linear interpolation scheme when viscosity is constant throughout the domain. For this case we confirm numerically that

the operators from (54) (which is the Galerkin coarse grid approximation) are identical within the machine accuracy to those constructed with (14) applied at all grid levels (which is the discretization coarse grid approximation), just as expected (e.g., Wesseling, 1992). Thus, the matrix dependent transfer multigrid algorithm with our interpolation scheme and coarse grid operators, with restriction operators determined with (54) and (53), always reduces to the standard multigrid method when viscosity is constant throughout the domain, while the Schur complement method does not.

We use a saw-tooth cycle to solve our convection problem. TABLE II lists a pseudo code for our implementation of the multigrid method. For smoothing we choose either line Jacobi with a relaxation parameter $\omega = 2/3$ or line Gauss-Seidel relaxation with red-black ordering (i.e., zebra ordering) with $\omega = 1.5$. Line relaxations are considered to give better convergence behavior than point relaxations and, therefore, we use line relaxations. Line relaxations are performed in either the vertical or horizontal direction. Smoothing is performed $\nu = 4$ times in the upward cycle. TABLE II

4 Multigrid Convergence Tests

For numerical experiments, we assume a Newtonian rheology with viscosity depending on temperature only:

$$\mu = \mu_0 \exp\left[a\frac{E}{R}\left(\frac{1}{T} - \frac{1}{T_1}\right)\right] \tag{56}$$

where μ_0 is a constant set to 10^{21} Pa sec, a is a scale factor, $R = 8.3143$ J K^{-1} mole^{-1} is the gas constant, and E is the activation energy set to 532.12 kJ mole^{-1} (for which E/R is 64,000 K) and T_1 is a constant set to 1300 K. All the cases we report in this section use the input parameters listed in TABLE III . For the mechanical boundary conditions, all four boundaries are chosen to be reflective. The bottom boundary is maintained at constant temperature of 2300 K and the top boundary is at constant 300 K. This represents a TABLE III

volume heated from below and cooled from top. For the viscosity value at $T = T_1$, the Rayleigh number is 1.163×10^6. Some of the parameter values deviate from those estimated for the Earth's mantle in order that our computational mesh be able to resolve the developing flow structure when the proper amount of viscosity variation is allowed. In fact, for extreme variations in viscosity in some of the cases we present, even this choice of convection parameters will not allow the mesh to resolve the flow structures in the regions of lowest viscosity (i.e., the area of a very high local Rayleigh number), and the numerical solution, a discretized approximation to the true analog solution, may not represent the analog solution very well. It should be noted, however, that the primary purpose of the tests presented in this section lies in identifying a robust way to solve a matrix equation set that represents the momentum equation at a given instant of time without regard to whether the given mesh can actually resolve the flow dynamics.

The depth-dependent reference temperature, $T_0(y)$, is assumed as

$$T_0(y) = \begin{cases} 2300 - 400\,\dfrac{n_2}{h}\,y, & 0 < y < \dfrac{5h}{2n_2} \\ 1300, & \dfrac{5h}{2n_2} < y < h - \dfrac{5h}{2n_2} \\ 300 + 400\,\dfrac{n_2}{h}\,(h-y), & h - \dfrac{5h}{2n_2} < y < h \end{cases} \tag{57}$$

where temperature is in K when y is in km.

The first test case presented has initial temperature field given by

$$T(x,y) = T_0(y) + 0.03\,T_0(h/2)\cos\frac{\pi x}{w}. \tag{58}$$

This temperature field represents a single roll structure, with a hot upwelling on the left side of the domain and a cold downwelling on the right side. The viscosity field is specified according to (56) with an appropriate choice for value a. A viscosity field corresponding to $a = 0.2$ is presented in FIGURE 4 (a). Most of viscosity variations occur near the both boundaries. layers.

FIGURE 4

A multigrid solution to (26) for this viscosity field is sought and convergence behavior is examined for two multigrid strategies: the standard method (i.e., the multigrid method with the discretization coarse grid approximation and the linear interpolation scheme) and the matrix-dependent transfer scheme coupled with the Galerkin coarse grid approximation outlined in the previous section. The former method will be labeled in this section with prefix 'D' and the latter with 'G'. For the discretization coarse grid approximation, the coarse grid viscosity value at a given point is computed by taking the arithmetic average of the neighboring fine grid values.

To quantify the convergence behavior for the various flavors of our two multigrid strategies we define a convergence rate as follows:

$$\text{convergence rate} = \left[\frac{\|\mathbf{r}^{(i)}\|}{\|\mathbf{r}^{(0)}\|} \right]^{1/i} \tag{59}$$

where i is the multigrid iteration number for which the residual $\|\mathbf{r}^{(i)}\|$ falls below 10^{-10} times the initial residual $\|\mathbf{r}^{(0)}\|$ (if residuals do not decrease fast enough, i is set to 20). TABLE IV lists the convergence rate for the discretization coarse grid formulation with vertical line Jacobi (DVJ), horizontal line Jacobi (DHJ), vertical line Gauss-Seidel with zebra ordering (DVGS) and horizontal line Gauss-Seidel with zebra ordering (DHGS). The table also lists the convergence rate for the Galerkin coarse grid formulation and the matrix-dependent transfer with vertical and horizontal line Jacobi (GVJ and GHJ, respectively), and vertical and horizontal line Gauss-Seidel with zebra ordering (GVGS and GHGS, respectively). Viscosity fields with $a = 0.0$, 0.1 and 0.2 are used for this test ($a = 0$ corresponds to constant viscosity). TABLE IV

FIGURE 5 plots residuals with respect to multigrid iteration number for a few selected cases and demonstrates an almost constant convergence rate over multigrid iterations. The table and figure demonstrate that the standard multigrid method generates a solution with a good convergence rate only for nearly constant viscosity field. Selection of other relaxation methods for this multigrid method is unlikely to alter the conclusion. On the FIGURE 5

other hand, the Galerkin coarse grid approximation yields by contrast much improved convergence rates. When it is combined with the line Gauss-Seidel relaxation (GVGS or GHGS), the solver provides an almost constant convergence rate for all range of a. The choice of the direction in line relaxations (i.e., vertical vs. horizontal) makes some differences only when a line Jacobi is chosen as a smoother for the Galerkin coarse grid formulation; it is seen in general that the smoothing direction makes little difference in terms of convergence behavior.

The test cases just presented contain a long wavelength lateral thermal structure and therefore a viscosity field which varies smoothly in the horizontal direction. It is not apparent how the algorithms might perform when there are many short wavelength fluctuations both vertically and horizontally in the viscosity field. To test the algorithms against more severe situations that contain strong short wavelength fluctuations both vertically and horizontally in the viscosity field we specify an initial temperature field given by

$$T(x,y) = T_0(y)\left[\left(1-\frac{b}{2}\right)+b\,r\right] \tag{60}$$

where b is a number between 0 and 1 and r is a random number between 0 and 1 generated with a uniform deviate using the method described in Press, Teukolsky, Vetterling and Brian (1992). We seek to test multigrid convergence behavior for viscosity fields generated with a in (56) set to 0.19 and b set to 0.2, 0.3, or 0.4, which correspond to random lateral temperature fluctuations of 20, 30 or 40 % in $T_0(y)$, respectively. For such temperature fields, the maximum viscosity contrast is given approximately by 10^C where

$$C = \frac{aE}{R\ln 10}\left[\frac{1}{500\,(1-b/2)}-\frac{1}{2100\,(1+b/2)}\right]. \tag{61}$$

Maximum lateral viscosity contrast at y is given approximately by $10^{c(y)}$ where

$$c(y) = \frac{aE}{R\ln 10}\left(\frac{1}{1-b/2}-\frac{1}{1+b/2}\right)\frac{1}{T_0(y)}. \tag{62}$$

C and $c(y)$ with $a = 0.19$ for different b are provided in TABLE V. To get a glimpse of sort of viscosity variations utilized in these tests one may refer to FIGURE 4 (b) which shows the viscosity field for $b = 0.3$. TABLE V

The convergence test results are provided in TABLE VI and residuals for DVJ, DVGS, GVJ and GVGS are plotted in FIGURE 6. As expected, solutions obtained with the discretization coarse grid formulation and the linear interpolation scheme exhibit poor convergence behavior with a convergence rate of 0.7 or larger. On the other hand, the matrix-dependent transfer yields solutions with good convergence rates for this extremely variable viscosity field. It is noteworthy that convergence rates remain almost constant for different values of b. For the extremely varying viscosity field for $b = 0.4$ the convergence rate with the line Gauss-Seidel relaxations is still less than 0.1, demonstrating that the matrix-dependent transfer algorithm presented in the previous section coupled with line Gauss-Seidel relaxation appears to represent an excellent candidate for solving the momentum equation with strongly variable viscosity. The table (also TABLE IV) demonstrates also that although the line Jacobi method in general yields inferior performance relative to the line Gauss-Seidel method, it nevertheless yields dramatically better performance when used with matrix-dependent transfer than any relaxation method with standard multigrid. TABLE VI FIGURE 6

On a single processor HP-UX 9000 workstation a V cycle multigrid iteration with the GVGS strategy can be completed in about 0.16 CPU second for $n_1 = n_2 = 64$, about 0.64 second for $n_1 = n_2 = 128$, and about 2.91 seconds for $n_1 = n_2 = 256$, when calculations are done with double precision. This statistics confirms a known multigrid property that CPU time taken in solving a matrix equation increases linearly with the order of the matrix. We find that for the random field problem the convergence rates are 0.083, 0.087 and 0.087, respectively for the three grids, indicating convergence behavior worsens slightly with increasing resolution.

Assembling forward operators and preparing inverse matrices for line relaxations at all grid levels can be accomplished within relatively little CPU time. On the same workstation it takes about 0.11 CPU second for $n_1 = n_2 = 64$, about 0.48 second for $n_1 = n_2 = 128$,

and about 1.95 seconds for $n_1 = n_2 = 256$ to assemble differential operators, determine weights and compute inverse matrices for line relaxations at all levels, which is slightly less than the time taken in completing one V cyle multigrid iteration.

5 Thermal Convection with Linear and Nonlinear Rheologies

In this section we report simulation results for time dependent thermal convection in an internally heated domain when viscosity is dependent on temperature, strain rate and yield stress. Newtonian dynamic viscosity is given by

$$\mu_N = \mu_0 \exp\left[a\frac{E}{R}\left(\frac{1}{T} - \frac{1}{T_1}\right)\right], \tag{63}$$

where μ_0 in this case is the viscosity value at $T = T_1$. By non-Newtonian rheology we will refer to a composite model where effective dynamic viscosity is given by

$$\mu_C = \frac{\mu_N \mu_P}{\mu_N + \mu_P} \tag{64}$$

when power-law viscosity μ_P is given by

$$\mu_P = \mu_0 \left(\frac{\dot{\varepsilon}}{\dot{\varepsilon_0}}\right)^{\frac{1}{n}-1} \exp\left[a\frac{E}{nR}\left(\frac{1}{T} - \frac{1}{T_1}\right)\right], \tag{65}$$

where $\dot{\varepsilon}$ is a square root of determinant of the strain rate tensor (which is the second invariant of this tensor of rank 2), $\dot{\varepsilon_0}$ is a constant in units of strain rate and n is power-law the exponent. For power-law rheology, μ_0 is the viscosity value when $T = T_1$ and $\dot{\varepsilon} = \dot{\varepsilon_0}$. μ_0 in (63) and (65) is assumed the same. For non-Newtonian rheology cases where viscosity is given by (64), μ_0 is the viscosity value when $T = T_1$ and $\dot{\varepsilon} \to 0$.

Dynamic viscosity μ, whether it is Newtonian or non-Newtonian, is limited in the

calculations within the range

$$\mu_{\min} \leq \mu \leq \mu_{\max}. \tag{66}$$

The maximum viscosity value $\mu_{\max}$ is introduced because the yield strength of the Earth's rocks is finite. For example, the unconfined compressive strength of gabbro and peridotite is about 200 MPa and unconfined tensile strength of gabbro is 20 MPa at room temperature (Lockner, 1995). The maximum viscosity value attained in the mantle, therefore, needs to be restricted in terms of a finite yield stress as the brittle elastic rock strength can be considered as a upper bound of stress in the ductile mantle. On the other hand the minimum viscosity $\mu_{\min}$ is introduced since thermal structures for very small viscosity cannot be adequately resolved with a given finite number of nodes.

In the simulation results presented below $\mu_{\max}$ is defined in two ways. One set of calculations is done with $\mu_{\max}$ set simply to $10^9\mu_0$ in both (63) and (65). This set of results will be loosely referred to have 'infinite' yield stress. The other set of results is obtained, defining the maximum value through finite yield stress τ_Y of the mantle materials:

$$\mu_{\max} = \frac{\tau_Y}{2\,\dot{\varepsilon}}. \tag{67}$$

In the brittle deformation regime material strength increases almost linearly with normal stress following the Byerlee's friction law but approaches a constant value in ductile and plastic deformation regions (Evans and Kohlstedt, 1995). Byerlee's law may be applicable for confining pressures up to several hundred MPa or for depths of around 10 km. Since the resolution of the numerical mesh for the calculations is about 23 km, yield stress is treated as a constant throughout the viscous mantle. How viscosity in the rheology models examined in this study varies with temperature, strain rate and yield stress is shown in FIGURE 7. As shown in the figure, introduction of finite yield stress dramatically alters the topography of the viscosity-temperature-strain rate map in both Newtonian and non-Newtonian cases. Regions most affected by the yield stress are those of low temperature

FIGURE 7

and high strain rate which might be characteristic of subduction zones on the Earth. This suggests that a finite yield stress has the potential to play a crucial role in mantle dynamics especially in regions of cold lithosphere. We will examine in this section how the Newtonian and non-Newtonian rheology with inifite as well as finite yield stresses of 10, 50 and 100 MPa can affect convection styles.

The physical parameters used for calculations in this section are listed in TABLE VII. Periodic conditions are used for the side boundary of the box. We choose the reference viscosity μ_0 to be 4×10^{22} Pa sec for Newtonian cases and 4×10^{23} Pa sec for non-Newtonian cases. A Boussinesq equation of state is assumed for these internally heated cases, and no vertical heat flow is allowed at the bottom boundary. The Rayleigh number based on the reference viscosity μ_0 is 1.5×10^7 for Newtonian cases and 1.5×10^6 for non-Newtonian cases. A temperature field for two convecting cells, similar to the one given by (58) but with spatial wavelength of w, is used as the initial condition.

TABLE VII

First, we examine a Newtonian case with infinite yield stress. FIGURE 8 (a) shows snapshots of temperature and viscosity fields at the model time of 6.0 Ga. In general temperature-dependent Newtonian rheology yields a thick upper thermal boundary layer that is nearly immobile (Tackley, 1996; Yang, 1997). Because of the low efficiency of heat transport through the layer (primarily by conduction rather than by advection), thermal energy tends to accumulate just below the layer. As a result the average temperature is highest in this region and large thermal anomalies tend to form there (Yang, 1997). The figure shows that localized thermal instabilities having the form of 'drips' develop at the base of the cold boundary layer. Cold material dripping from the bottom of the boundary layer would tend to drag the boundary layer into the interior of the volume but high values of viscosity near the surface prevent this from occurring. The horizontal profiles of the surface velocity at the model times of 5.0 and 6.0 Ga, shown in FIGURE 9 (a), indicate the surface is moving at a uniform velocity. Since with the periodic side boundary condition the solution to the Navier-Stokes equations is unique only within an additive constant of the horizontal velocity component, the uniform surface velocity is equivalent to the immobile

FIGURE 8

surface. (For the periodic boundary condition we set the velocity values at the lower left and the lower right corners to zeroes.)

Mobility of the surface boundary layer, a characteristic of plate-like motion, can be estimated qualitatively from the average surface velocity with respect to the mass flux at a reference depth. For this we define the normalized surface velocity U and normalized mass flux $M(y)$ using the same normalization factor as

$$U = \frac{c_p}{k} \int_0^w \rho \left| u_x(x,h) \right| \, dx \tag{68}$$

$$M(y) = \frac{c_p}{k} \int_0^w \rho \left| u_y(x,y) \right| \, dx. \tag{69}$$

FIGURE 10 (a) displays time series of U and $M(y)$ at the mid-depth in the box of the Newtonian case. There is certainly sizable mass flux through the horizontal plane at the mid-depth. The average surface velocity, hovering between 0.1 and 4000, appears to be frequently comparable to the downwelling velocity. However, U reaching or exceeding M occasionally is simply an artifact of the periodic boundary condition. For example, at 5.0 Ga where there is a 'peak' in the time series of U, the surface is moving at a uniform velocity as can be seen in Figure 9 (a), which is equivalent to existence of immobile surface. Therefore, we can conclude that with the temperature-dependent Newtonian rheology the surface boundary layer barely moves.

FIGURE 10

FIGURE 8 (b) and (c) show two snapshots of the temperature and viscosity fields of the Newtonian case with a finite yield stress of 100 MPa at 10 and 12 Ga, respectively. Their respective horizontal profiles of the surface velocity can be found in FIGURE 9 (b) and (c). Clearly, the flow field at 12 Ga is the same in nature as that of a Newtonian case with the infinite yield stress. Time series of both U and M at the mid-depth, shown in FIGURE 10 (b), reveal that the fluid system remains in this type of regime until stress in the cold thermal boundary layer exceeds the yield stress. When this happens, viscosity decreases due to high strain rates in a few locations at the surface from which downwellings initiate. Downwellings occur in the form of series of catastrophic avalanches. The snapshot

at 10 Ga shows massive downwelling plume heads settled at the bottom of the box as a consequence of sudden avalanches. During these avalanches both the values of U and M are about 10,000 or larger (3 cm/yr or larger in dimensional quantities), which is about a 10-fold increase from the normal level mass flux. The surface velocity during avalanches displays a somewhat piecewise constant character. This is the regime claimed to be plate-like by Trompert and Hansen (1998), but identified as transitional between frozen and mobile lid regimes by Moresi and Solomatov (1998). After stress release the system returns to the regime where the surface becomes immobile.

FIGURE 8 (d) and (e) are for a yield stress of 50 MPa. Time series in FIGURE 10 (c) indicate that the system is significantly less catastrophic, compared to the case with τ_Y=100 MPa. However, episodic increases in downwelling material are still prevalent. The surface is now mobile and its average velocity is comparable to the downward velocity at the mid-depth all the time. As shown in FIGURE 9 (d) and (e), the surface velocity field is to a certain degree piecewise constant. This means that low viscosity weak zones are created at the top surface and they are sandwiched by high viscosity patches. We can visually identify such high viscosity patches in the snapshots that move as one unit.

When the yield stress is too small the surface can be weakened easily, because stress in the cold boundary layer can reach the yield stress limit quickly. Consequently downwellings occur very frequently. FIGURE 10 (d) shows time series for the Newtonian case with a yield stress of 10 MPa that illustrate this point clearly. The maximum amplitude of both average surface velocity and downward velocity can be larger than 100,000 (or velocity $\sim$ 30 cm/yr) during periodic avalanches. Since many locations at the surface can reach this low stress limit, it is also expected that downwellings will develop at many locations and, as a consequence, many small wavelength structures will be created during avalanches. FIGURE 8 (f) and (g) show the snapshots of temperature and viscosity fields at 1.0 (inter-avalanche period) and 1.7 Ga (avalanche period). The snapshot at 1.7 Ga indeed shows many small wavelength structures. Because of overall weakening the highest viscosity value at this time is only about 5×10^{25} Pa sec, significantly lower than the usual highest value

of more than 10^{30} Pa sec. The surface velocity field which is shown in FIGURE 9 (f) and (g), do not resemble plate velocity field, especially during avalanches.

The case of a non-Newtonian fluid exhibits a considerably different downwelling style from a Newtonian fluid. A snapshot is shown in FIGURE 8 (h). High stress serves to weaken the region where downwelling occurs. This lowers the viscosity and thereby mobilizes the otherwise sluggish high viscosity upper boundary layer. FIGURE 10 (e) shows that the surface is moving at a speed comparable to the downward velocity. The surface velocity profile, shown in FIGURE 9 (h), does not resemble a plate like velocity field.

When a finite yield stress of 100 MPa is introduced, the non-Newtonian case exhibits episodic avalanches of cold material. FIGURE 10 (f) shows increased fluctuations in both U and M. However, the avalanches are not as strong as those found in the Newtonian case with the same yield stress. FIGURE 8 (i) and (j) show snapshots of the temperature field at 3.5 and 4.0 Ga, respectively. As can be seen in FIGURE 9, the surface is mobile. We observe that at 4.0 Ga large high viscosity patches exist at the surface and move at a constant horizontal velocity, much like Earth's plates.

With $\tau_Y = 50$ MPa time series of U and M, shown in FIGURE 10 (g), show similar temporal patterns as the case with yield stress of 100 MPa. The surface velocity profiles, FIGURE 9 (k) and (l), once again show some piecewise constant character. Temperature and viscosity fields at the corresponding times are shown in FIGURE 8 (k) and (l). Once again we can recognize a few high viscosity patches at the surface which are moving at a uniform horizontal velocity.

When yield stress is 10 MPa, the surface can be weakened easily and quickly. As in the Newtonian rheology case with the same yield stress, we expect many small wavelength structures to flourish. The snapshots shown in FIGURE 8 (m) and (n) are in general consistent with this expectation. The horizontal profiles of the surface velocity in FIGURE 9 (m) and (n) display some plate-like character. Unlike the Newtonian counterpart, both U and M have smaller peaks in the time series, as shown in FIGURE 10 (h).

It can be noticed that, in order to have a plate-like surface velocity field, large high viscosity patches need to exist at the surface, flanked on each side by a low viscosity weak zone. These patches, then, will move along the surface at constant velocities. When the yield stress is too large, there are occasional strong avalanches during which the model displays a plate-like velocity field. However, after avalanches the top lid is frozen in a Newtonian case. The system is highly unsteady. On the other hand, when the yield stress is low, the surface becomes weak all the time, and only small isolated high viscosity patches exist. In this case a plate-like velocity field is recognized only in those small patches, separated by small wavelength downwellings. Between these two extremes we observe a system exhibiting plate-like patches with somewhat clear boundaries consistently throughout the whole time, even though the system exhibits episodic avalanches of downwellings of cold material to the bottom of the box. The range of yield stress for this regime is found to be between 10 and 100 MPa (around 50 MPa) with both Newtonian and non-Newtonian rheology for the input parameters used. Non-Newtonian rheology appears to have a wider range of yield stress values for this regime than Newtonian rheology. This regime is probably closest to the Earth's plate regime that we can produce using this rather simple model, which does not consider many important geophysical effects such as partial melting, phase changes, a more geophysically relevant depth-dependent viscosity and brittle deformation at the surface.

6 Conclusions

It is well known that the standard multigrid method, which uses linear interpolation for transfering residual and correction vectors between different grid levels and adopts the discretized coarse grid approximation, is not efficient when differential equations contain highly variable coefficients. Matrix-dependent transfer, in which interpolation and restriction operators are derived in terms of a given differential operator, is an effective means for addressing this problem. We demonstrate the generality of this approach in this study

where we extend the matrix-dependent transfer multigrid algorithm to the 2-D tensor differential operator case. The method presented here is well suited to solving thermal convection and other fluid mechanical problems with strongly variable viscosity. Line Gauss-Seidel smoothing with a zebra ordering, both horizontal and vertical, is found to be a very effective relaxation method in obtaining convergent solutions for the momentum equation, although vertical relaxation is favored for large aspect ratio problems. Application of this method allows us to address very difficutl questions about the role of rheology in governing plate tectonics and mantle convection.

The numerical simulations in the previous section demonstrate that a variety of convection styles can exist for different rheology models, and for different values of yield stress. We find that with a finite yield stress infinite Prandtl number flow may exhibit episodic avalanching of cold material from the upper boundary layer to the bottom of the domain. The intensity of this behavior depends on the yield stress and the strength of the power-law component in the rheological model. As the yield stress value is lowered, Newtonian cases go through a transition from a rigid lid convection style, to an episodically avalanching style, to a regime where the surface boundary layer becomes mobile with less catastrophic downwellings and then finally to another avalanche regime where the small wavelength structures are created by frequent and strong avalanches of downwellings. The transitions down to the regime where the surface becomes mobile are also observed by Moresi and Solomatov (1998) using Newtonian rheology. Non-Newtonian cases, on the other hand, stay generally in a regime where the surface is mobile for all the yield stress values examined (10–100 MPa). With the input model parameters in TABLE VII, we find with both Newtonian and non-Newtonian rheology that the top boundary layer is mobile and has a somewhat plate-like piecewise constant velocity field at the surface consistently throughtout numerical simulations for yield stresses between 10 and 100 MPa.

In order to see how a particular rheology law and a finite yield stress operates in the formation of weak zones and mobile lids, we consider plots of viscosity with respect to strain-rate along isotherms of 500, 1000 and 1500 K. The plots in FIGURE 11 are the

FIGURE 11

projections of the three-dimensional plots in FIGURE 7 onto the viscosity and strain-rate plane along these isotherms. FIGURE 11 (a) shows three viscosity values at the three isotherms (the viscosity value for 500 K, 8.7×10^{30} Pa sec, is not shown here). When stress is building up in the cold thermal boundary layer, viscosity remains the same and the surface remains immobile. When a finite yield stress is introduced, a viscosity value is limited by (67). Thus, when stress builds up at a point which remains on the isotherm of, for example, 1000 K, viscosity remains the same until strain rate reaches about 10^{-18} sec^{-1}. Once this value is reached, viscosity decreases inversely with strain-rate following the sloping line in FIGURE 11 (b). We can note from this figure that this cross-over strain-rate value decreases with temperature, which means that cold regions at the surface start to weaken at a smaller strain-rate value.

We can also observe that, with non-Newtonian rheology, cold regions are those affected most by a finite yield stress. Since an increase in stress is accompanied by a decrease in viscosity, the surface can become mobile. This reduction of viscosity with stress build up is probably what prevents the non-Newtonian case with yield stress of 100 MPa from forming a series of catastrophic avalanches of downwellings which are present in the Newtonian case with the same yield stress. Without this self weakening mechanism, the surface remains stiff until the yield stress effect takes over and the stored stress is released in a catastrophic manner. FIGURE 11 (d) shows that only the isotherm of 500 K is affected by a finite yield stress. On this isotherm the yield stress effect is felt when strain-rate reaches about 10^{-16} sec^{-1}. Although the figure gives an impression that the effect of finite yield stress is small in case of non-Newtonian cases, it still plays an important role just as we have witnessed in the previous section. The cross-over point exists as long as $0 \geq 1/n - 1 > -1$ or $n \geq 1$, which means that a physically meaningful rheology model cannot avoid finite yield stress effects.

Regions most affected by yield stress in the Earth are likely subduction zones where temperature is low and strain-rate is high. This suggests that finite strength likely plays a very important role in the formation of plates and their dynamic interactions, in addition

to ensuing brittle deformation. We find in Newtonian cases that cold regions start to weaken first. This suggests an explanation of how formation of a weak zone might be initiated in the upper boundary layer. The boundary layer is weakened in a cold region first which experiences a viscosity reduction even for small strain-rate. Once such a weak zone develops, the strain-rate starts to grow in the neighboring region, which then brings a viscosity reduction for a warmer region as well. In the case of non-Newtonian rheology formation of a weak zone does not necessarily have to start from the coldest region, because both cold and warm regions can be sites of high strain rate and reduced viscosity.

We have used our new methodology in several example calculations under Earth-like conditions. We find that even relatively simple models with large aspect ratio, internal heating, physical parameters (e.g., viscosity) similar to Earth's mantle, and including a finite yield stress can result in extremely episodic flow and heat transport, as well as plate-like surface boundary layer velocities. These examples were designed mainly to illustrate the power of the numerical method, but they suggest that many possible exotic behaviors of the mantle convection system have yet to be discovered. A key question for future studies will be the degree to which a finite yield stress, or some other strain rate weakening rheology, forms a reasonable simulation of actual plate boundaries in the Earth. As resolution in computer models increases and 3-D calculations are performed, the signficant differences between true fracture mechanics and plastic yielding should become more apparent. Methodologies such as that developed here should allow for such studies in the near future.

References

Alcouffe, R. E., Brandt, A., Dendy, J. E. Jr. and Painter, J. W., "The multi-grid method for the diffusion equation with strongly discontinous coefficients", *SIAM J. Sci. Stat. Comput.* **2**, 430–454 (1981).

Baumgardner, J. R., *A Three-dimensional Finite Element Model for Mantle Convection*, PhD thesis, UCLA (1983).

Baumgardner, J. R., "Three-dimensional treatment of convective flow in the Earth's mantle", *J. Stat. Phys.* **39**, 501–511 (1985).

de Zeeuw, P. M., "Matrix-dependent prolongations and restrictions in a blackbox multigrid solver", *J. of Computational and Applied Mathematics* **33**, 1–27 (1990).

Evans, B. and Kohlstedt, D. L., "Rheology of rocks", *in* T. J. Ahrens, ed., *Rock Physics & Phase Relations: A Handbook of Physical Constants*, American Geophysical Union, Washington D. C., pp. 148–165 (1995).

Glatzmaier, G. A., "Numerical simulations of mantle convection: time-dependent, three-dimensional, compressible, spherical shell", *Geophys. Astrophys. Fluid Dynamics* **43**, 223–264 (1988).

Hackbusch, W., "Multi-grid convergence theory", *in* W. Hackbusch and U. Trottenberg, eds, *Multigrid Methods, Proceedings of the Conference, Köln-Porz, 1981*, Lecture Notes in Mathematics 960, Springer-Verlag, pp. 177–219 (1982).

Jarvis, G. T. and McKenzie, D. P., "Convection in a compressible fluid with infinite Prandtl number", *J. Fluid Mech.* **96**, 515–583 (1980).

Karato, S. and Wu, P., "Rheology of the upper mantle: a synthesis", *Science* **260**, 771–778 (1993).

Kettler, R., "Analysis and comparison of relaxation schemes in robust multigrid and preconditioned conjugate gradient methods", *in* W. Hackbusch and U. Trottenberg, eds,

Multigrid Methods, Proceedings of the Conference, Köln-Porz, 1981, Lecture Notes in Mathematics 960, Springer-Verlag, pp. 502–534 (1982).

Lockner, D. A., "Rock failure", *in* T. J. Ahrens, ed., *Rock Physics & Phase Relations: A Handbook of Physical Constants*, American Geophysical Union, Washington D. C., pp. 127–147 (1995).

Moresi, L. and Solomatov, V., "Mantle convection with a brittle lithosphere: thoughts on the global tectonic styles of the Earth and Venus", *Geophys. J. Int.* **133**, 669–682 (1998).

Patankar, S. V., *Numerical Heat Transfer and Fluid Flow*, Hemisphere Pub. Corp., Washington (1980).

Press, W. H., Teukolsky, S. A., Vetterling, W. T. and Brian, P., *Numerical Recipes in Fortran 77: The Art of Scientific Computing*, second edn, Cambridge University Press, Cambridge (1992).

Ramage, A. and Walthan, A. J., "Iterative solution techniques for finite element discretizations of fluid flow problems", *in Proceedings of the Copper Mountain Conference on Iterative Methods, Copper Mountain, Colorado, 1992*, Vol. 1 (1992).

Ranalli, G., "The microphysical approach to mantle rheology", *in* R. Sabadini, K. Lambeck and E. Boschi, eds, *Glacial Isostasy, Sea Level and Mantle Rheology*, Kluwer Academic Publishers, Dordrecht, pp. 343–378 (1991).

Reusken, A., "Multigrid with matrix-dependent transfer operators for a singluar perturbation problem", *Computing* **50**, 199–211 (1993).

Reusken, A., "Multigrid with matrix-dependent transfer operators for convection-diffusion problems", *in* P. W. Hemker and P. Wesseling, eds, *Multigrid methods IV, Proceedings of the Fourth European multigrid conference, Amsterdam, 1993*, Birkhauser Verlag, Basel (1994).

Stocker, R. L. and Ashby, M. F., "On the rheology of the upper mantle", *Rev. Geophys. Space Phys.* **11**, 391–426 (1973).

Tackley, P. J., "Effects of strongly variable viscosity on three-dimensional compressible convection in planetary mantle", *J. Geophys. Res.* **101**, 3311–3332 (1996).

Trompert, R. and Hansen, U., "Mantle convection simulations with rheologies that generate plate-like behavior", *Nature* **395**, 686–689 (1998).

Turcotte, D. L., Torrance, K. E. and Hsui, A. T., "Convection in the Earth's mantle", *Meth. Comp. Physics* **13**, 431–451 (1973).

van Leer, B., "Towards the ultimate conservative difference scheme. V. A second-order sequel to Godunov's method", *J. Comp. Phys.* **32**, 101–136 (1979).

Wagner, C., "A multigrid method with matrix-dependent transfer operators applied in groundwater science", *in* A. Peters, G. Wittum, B. Herrling, U. Meissner, C. A. Brebbia, W. G. Gray and G. F. Pinder, eds, *Computational Methods in Water Resources X*, Vol. 2, Kluwer Academic Publishers, Dordrecht, pp. 1439–1446 (1994).

Weertman, J., "The creep strength of the Earth's mantle", *Rev. Geophys. Space Phys.* **8**, 145–168 (1970).

Weertman, J. and Weertman, J. R., "High temperature creep of rock and mantle viscosity", *Ann. Rev. Earth Planet Sci.* **3**, 293–315 (1975).

Wesseling, P., *An Introduction to Multigrid Methods*, John Wiley & Sons, Inc., Chichester (1992).

Yang, W., *Variable Viscosity Thermal Convection at Infinite Prandtl Number in a Thick Spherical Shell*, PhD thesis, University of Illinois at Urbana-Champaign (1997).

TABLE I The overall procedure to solve for $\mathbf{u}$, p and T for a given time. The conjugate method as outlined by Ramage & Walthan (1992) is used for the inner loop to solve (11) and (12) simultaneously. The outer loop is to repeat this procedure and solving for T to find a solution set simultaneously satisfying all the governing equations.

Set $u_0 = \|\mathbf{u}\|$ with initial guess $\mathbf{u}$
for $j = 1, N_2$ do
  Solve $A\mathbf{u}_0 - Gp_0 = \mathbf{f}$ for $\mathbf{u}_0$ with initial guess $p = p_0$
  Evaluate residual, $r_0 = G^T\mathbf{u}_0$
  for $i = 1, N_1$ do
    if $(i = 1)$ then
      $s_1 = r_0$
    else
      $\delta = \dfrac{\langle r_{i-1}, r_{i-1}\rangle}{\langle r_{i-2}, r_{i-2}\rangle}$
      $s_i = r_{i-1} + \delta \cdot s_{i-1}$
    end if
    Solve $A\mathbf{v}_i = Gs_i$ for $\mathbf{v}_i$
    $\alpha = -\dfrac{\langle r_{i-1}, r_{i-1}\rangle}{\langle s_i, G^T\mathbf{v}_i\rangle}$
    $p_i = p_{i-1} + \alpha s_i$
    $\mathbf{u}_i = \mathbf{u}_{i-1} + \alpha\mathbf{v}_i$
    $r_i = r_{i-1} + \alpha G^T\mathbf{v}_i$
    if $(\|r_i\| < \varepsilon_d)$ exit loop
  end
  Set $\mathbf{u} = \mathbf{u}_{N_1}$ and $p = p_{N_1}$
  Solve energy equation for T
  $u_j = \|\mathbf{u}\|$
  if $(|u_j - u_{j-1}| < \varepsilon_u u_0)$ exit loop
end

TABLE II A saw-tooth cycle multigrid algorithm to solve $A^n\mathbf{u} = \mathbf{b}^n$ where the superscripts refer to the grid level. $\mathcal{S}^\nu(\mathbf{e}^k, \mathbf{r}^k, \omega)$ refers to the solution (i.e., an estimate for $\mathbf{e}^k$) obtained after relaxing ν times on $A^k\mathbf{e}^k = \mathbf{r}^k$ with a relaxation parameter ω at the k-th level with initial guess $\mathbf{e}^k = \mathbf{0}$. Initial guess for $\mathbf{u}$ is the solution of the last time step of this time dependent system or $\mathbf{0}$ if it is for the first time step. For the test cases presented $\nu = 4$ is used. $\omega = 2/3$ is used for a line Jacobi relaxation and $\omega = 1.5$ is used for a Gauss-Seidel relaxation with zebra ordering.

---

for $i = 1, N$ do
  $\mathbf{r}^n = \mathbf{b}^n - A^n\mathbf{u}$
  $r = \|\mathbf{r}^n\|$
  for $k = n, 1, -1$ do
    $\mathbf{r}^{k-1} = R^{k-1,k}\mathbf{r}^k$
  end
  $\mathbf{z}^0 = (A^0)^{-1}\mathbf{r}^0$
  for $k = 1, n-1$ do
    $\mathbf{z}^k = P^{k,k-1}\mathbf{z}^{k-1}$
    $\mathbf{r}^k = \mathbf{r}^k - A^k\mathbf{z}^k$
    $\mathbf{z}^k = \mathbf{z}^k + \mathcal{S}^\nu(\mathbf{e}^k, \mathbf{r}^k, \omega)$
  end
  $\mathbf{u} = \mathbf{u} + P^{n,n-1}\mathbf{z}^{n-1}$
  $\mathbf{r}^n = \mathbf{b}^n - A^n\mathbf{u}$
  $\mathbf{u} = \mathbf{u} + \mathcal{S}^\nu(\mathbf{e}^n, \mathbf{r}^n, \omega)$
  if $(r < \varepsilon_r \|\mathbf{b}^n\|)$ exit loop
end

TABLE III Thermodynamic input parameters used for multigrid convergence test.

width, w	2890 km
thickness, h	2890 km
horizontal resolution parameter, n_1	128
vertical resolution parameter, n_2	128
density, ρ, $\rho 0$	3400 kg m^{-3}
gravitational acceleration, g	10 m sec^{-2}
thermal expansion coefficient, α	2.5×10^{-5} K^{-1}
thermal conductivity, k	120 W m^{-1} K^{-1}
specific heat, c_p, c_V	10^3 J kg^{-1} K^{-1}
Grüneisen parameter, γ	0
heat generation rate, H	0 W kg^{-1}
K/μ	1/3

TABLE IV Convergence rates obtained using various multigrid algorithms with different smoothers for the first group of cases with viscosity scale factor a set to 0, 0.1, 0.2 and 0.3. DVJ, DHJ, DVGS and DHGS are the discretization coarse grid approximation with the linear interpolation scheme using, as a smoother, a vertical line Jacobi, a horizontal line Jacobi, a vertical line Gauss-Seidel with zebra ordering and a horizontal line Gauss-Seidel with zebra ordering, respectively. GVJ, GHJ, GVGS and GHGS are the matrix-dependent transfer with the Galerkin coarse grid approximation using the same group of smoothers.

	$a = 0.0$	$a = 0.1$	$a = 0.2$
DVJ	0.083	0.663	0.759
DHJ	0.092	0.656	0.781
DVGS	0.071	0.290	0.635
DHGS	0.091	0.332	0.674
GVJ	0.083	0.128	0.202
GHJ	0.092	0.095	0.096
GVGS	0.071	0.073	0.074
GHGS	0.091	0.094	0.095

TABLE V C and $c(y)$ values in (61) and (62) for $b = 0.2$, 0.3 and 0.4 and $a = 0.19$.

	$b = 0.2$	$b = 0.3$	$b = 0.4$
top layer	2.134	3.242	4.401
second top layer	1.185	1.801	2.445
middle layers	0.821	1.247	1.693
second bottom layer	0.628	0.953	1.294
bottom layer	0.508	0.772	1.048
C	9.449	10.239	11.107

TABLE VI Convergence rates obtained using various multigrid algorithms with different smoothers for the second group of cases with a set to 0.19 and b set to 0.2, 0.3 and 0.4.

	$b = 0.2$	$b = 0.3$	$b = 0.4$
DVJ	0.760	0.812	0.859
DHJ	0.773	0.773	0.780
DVGS	0.601	0.785	0.890
DHGS	0.645	0.639	0.659
GVJ	0.156	0.159	0.158
GHJ	0.112	0.118	0.127
GVGS	0.084	0.087	0.088
GHGS	0.094	0.094	0.095

TABLE VII Input parameters used for simulations.

width, w	11560 km
thickness, h	2890 km
horizontal resolution parameter, n_1	512
vertical resolution parameter, n_2	128
density, ρ, $\rho 0$	3400 kg m^{-3}
gravitational acceleration, g	10 m sec^{-2}
thermal expansion coefficient, α	2.5×10^{-5} K^{-1}
thermal conductivity, k	4 W m^{-1} K^{-1}
specific heat, c_p, c_V	10^3 J kg^{-1} K^{-1}
Grüneisen parameter, γ	0
heat generation rate, H	5×10^{-12} W kg^{-1}
reference viscosity, μ_0	4×10^{22} Pa sec or 4×10^{23} Pa sec
minimum viscosity, $\mu_{\min}$	$0.01\mu_0$
viscosity variation scale factor, a	0.2
reference strain rate, $\dot{\varepsilon_0}$	10^{-19} sec^{-1}

FIGURE 1 The physical domain is discretized into $(n_1+1)\times(n_2+1)$ square mesh. The (x,y) coordinates of the lower left corner is $(0,0)$ and those of the upper right corner is (w,h).

FIGURE 2 Two-grid system, each with two layers of ghost nodes. The coarse grids are denoted by dots. Thick line indicates the boundary of the real physical domain ($0 < x < w$ and $0 < y < h$).

FIGURE 3 Two-grid configuration near the node whose fine grid index is (i_1, i_2) and coarse grid index is (I_1, I_2). Coarse grid nodes are marked with dots.

FIGURE 4 Viscosity field for $a = 0.25$ and $b = 0.4$. Logarithmic value with base 10 is plotted.

FIGURE 5 Residual ratios ($\|\mathbf{r}^{(i)}\|/\|\mathbf{r}^{(0)}\|$) with respect to multigrid iteration for a single roll temperature field when a is set to 0, 0.1, 0.2, and 0.3. (a) DVJ (b) DVGS (c) GVJ (d) GVGS. For notations see TABLE IV.

FIGURE 6 Residual ratios ($\|\mathbf{r}^{(i)}\|/\|\mathbf{r}^{(0)}\|$) with respect to multigrid iteration for a temperature field with random lateral fluctuations when a is set to 0.25 and b is set to 0.2, 0.3 and 0.4. For notations see TABLE IV.

FIGURE 7 Rheology models used in calculations. $a = 0.2$, $T_1 = 2000$ K, $n = 3$, $\dot{\varepsilon}_0 = 10^{-19}$ sec^{-1}. $\mu_0 = 4\times10^{22}$ Pa sec for Newtonian and 4×10^{23} Pa sec for non-Newtonian rheology. (a) Newtonian rheology (b) Newtonian rheology with $\tau_Y = 50$ MPa (c) non-Newtonian rheology (d) non-Newtonian with $\tau_Y = 50$ MPa.

FIGURE 8 Snapshots of temperature field during downwelling sequences. The times when the snapshots are taken are indicated by arrows in FIGURE 10. (a) A Newtonian case with 'infinite' τ_Y at $t = 8.10\times10^8$, 8.20×10^8, and 8.30×10^8 yr. (b) A non-Newtonian case with 'infinite' τ_Y at $t = 7.00\times10^8$, 7.08×10^8, and 7.24×10^8 yr. Due to an avalanche on thr right side of the box, the downwelling site near the center is dragged to the right. (c) A Newtonian case with $\tau_Y = 100$ MPa at $t = 7.21\times10^8$, 7.42×10^8, and 7.83×10^8 yr. Two avalanching events are observed, one each side of the box. (d) A non-Newtonian case with $\tau_Y = 100$ MPa at $t = 5.10\times10^8$, 5.18×10^8, and 5.22×10^8 yr. The most violent avalanche occurs near the center of the box.

FIGURE 9 Time series of normalized mass flux across the mid-depth of the mantle (M), normalized mean surface velocity (U) and the ratio (U/M). (a) Newtonian rheology (b) non-Newtonian rheology (c) Newtonian rheology with $\tau_Y = 100$ MPa (d) non-Newtonian with $\tau_Y = 100$ MPa. Three arrows in (a) and (b) indicate the times where the snapshots shown in FIGURE 8 are taken.

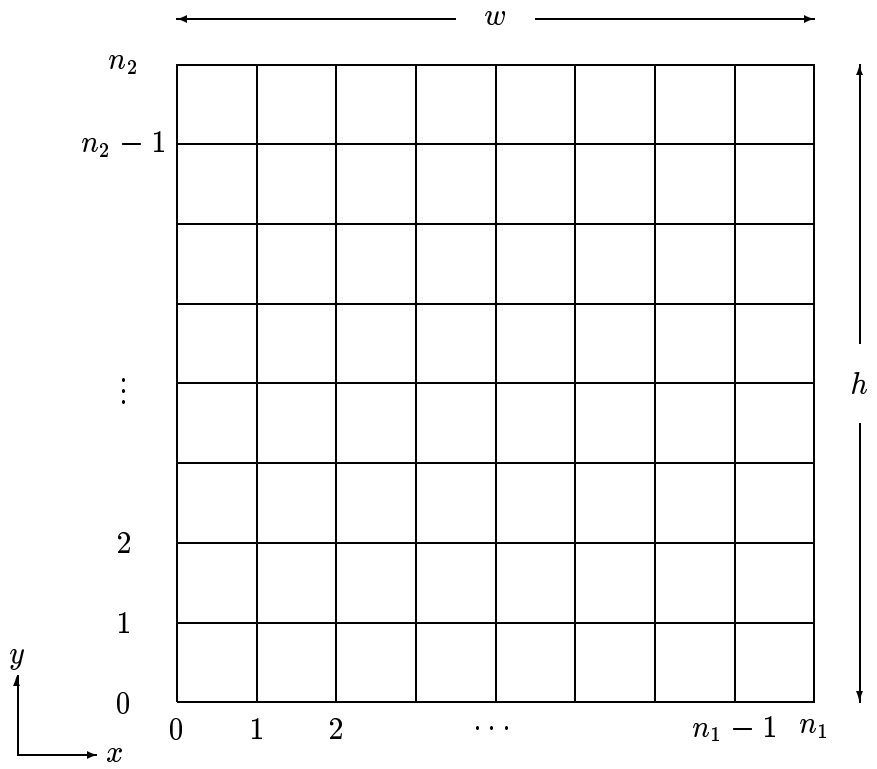

FIGURE 1 Woo-Sun Yang & J. R. Baumgardner

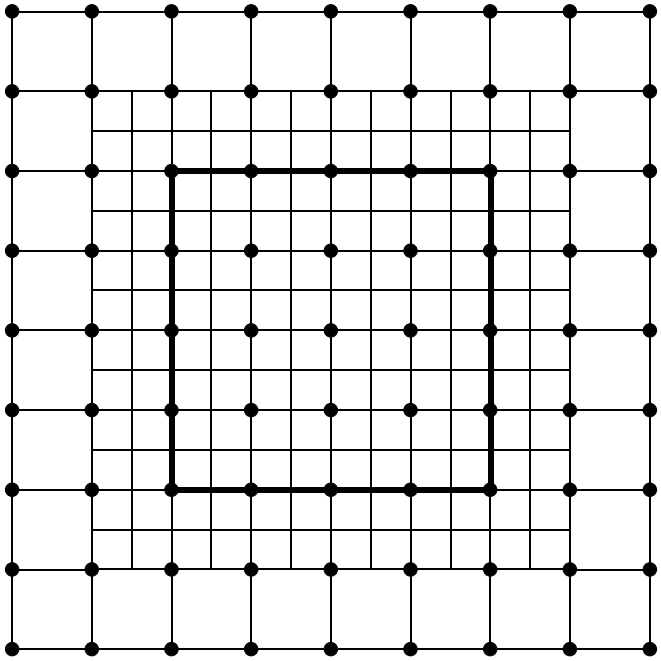

FIGURE 2 Woo-Sun Yang & J. R. Baumgardner

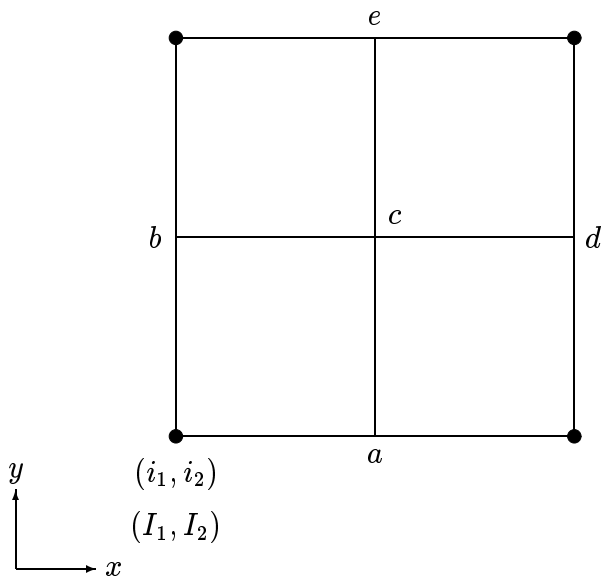

FIGURE 3 Woo-Sun Yang & J. R. Baumgardner

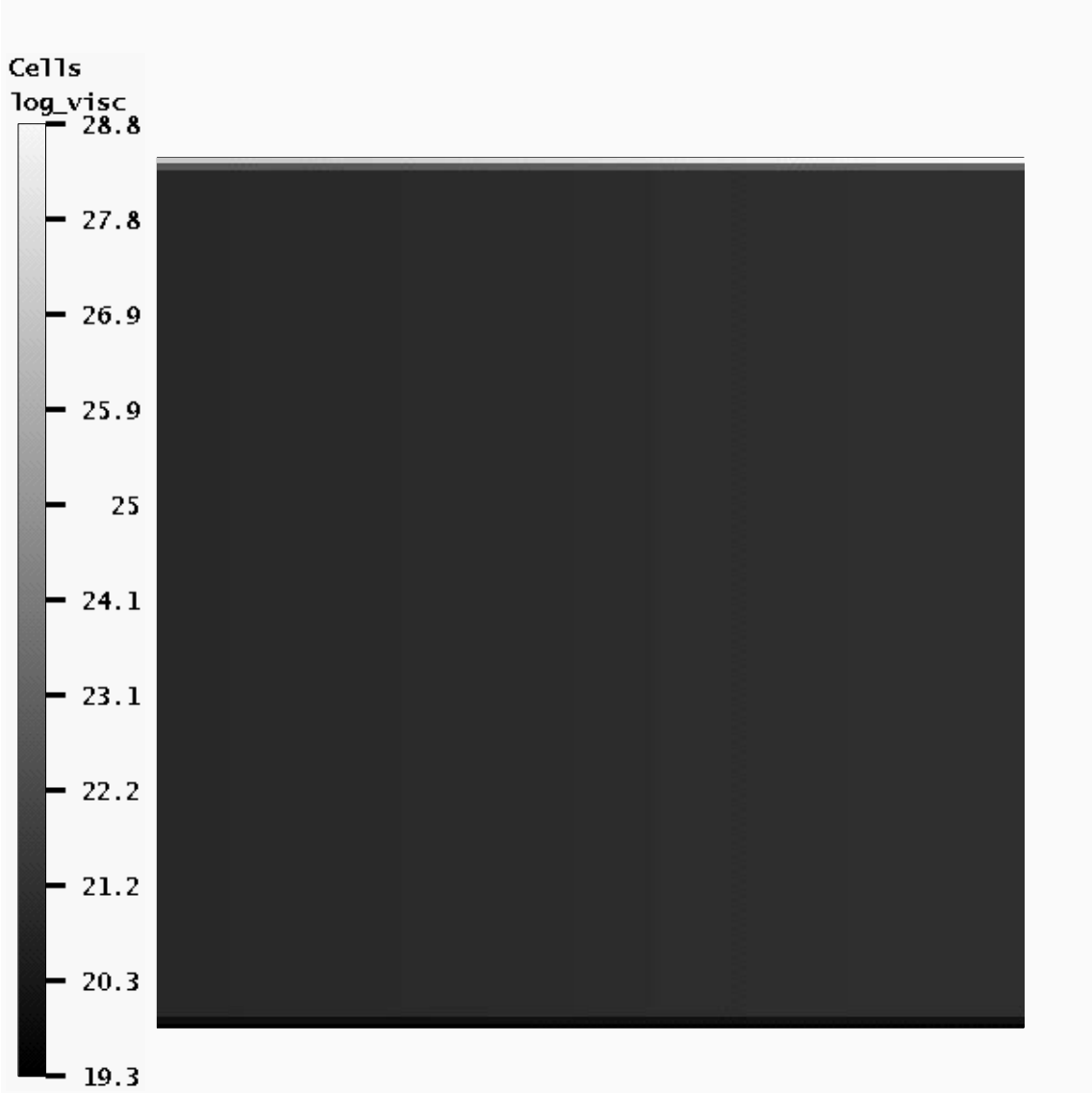

(a)

FIGURE 4 Woo-Sun Yang & J. R. Baumgardner

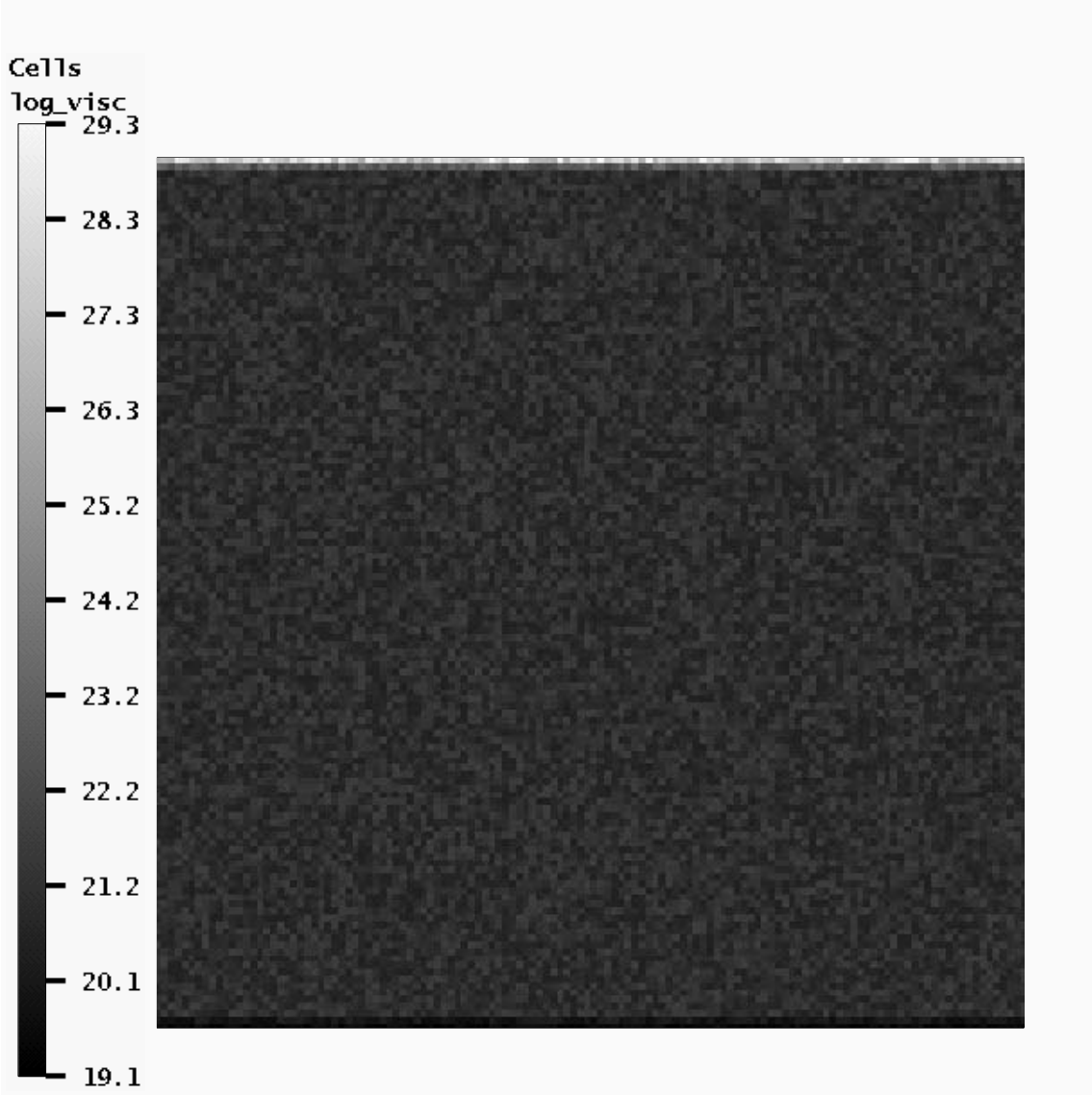

(b)

FIGURE 4 Woo-Sun Yang & J. R. Baumgardner

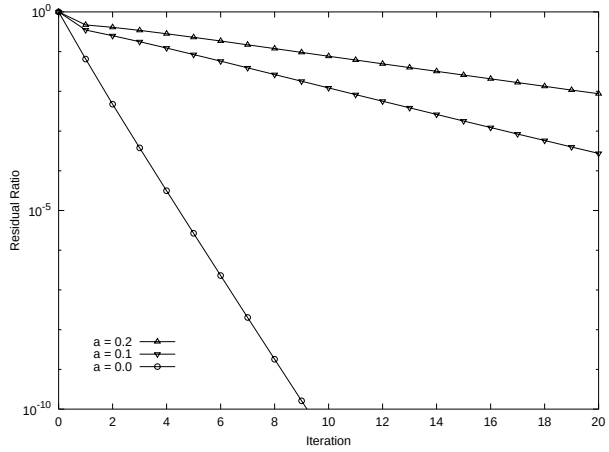

(a)

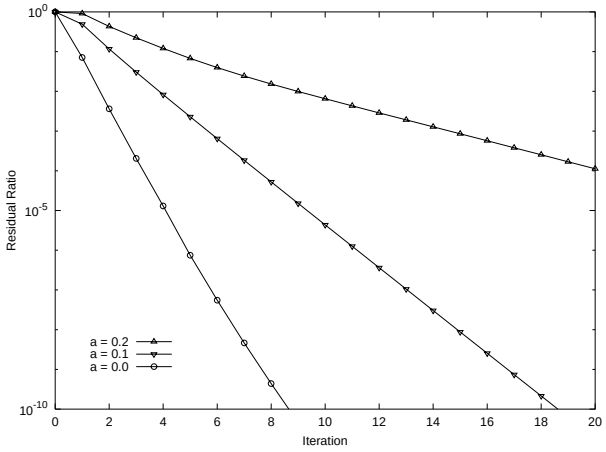

(b)

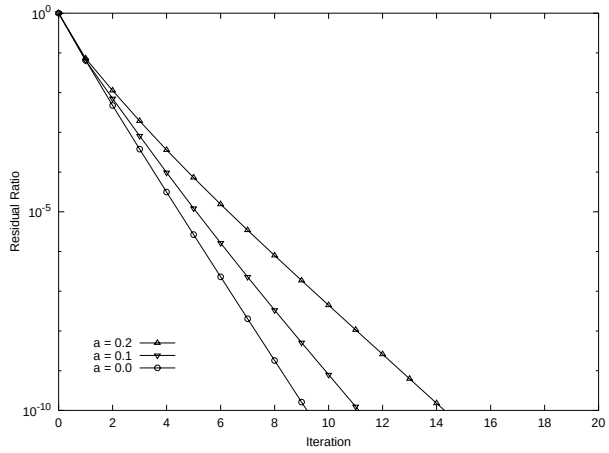

(c)

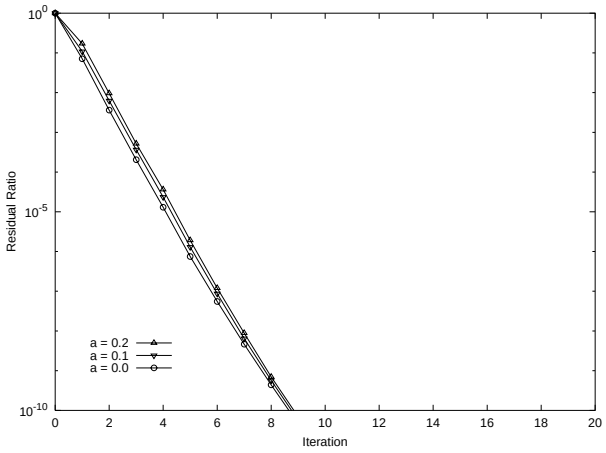

(d)

FIGURE 5 Woo-Sun Yang & J. R. Baumgardner

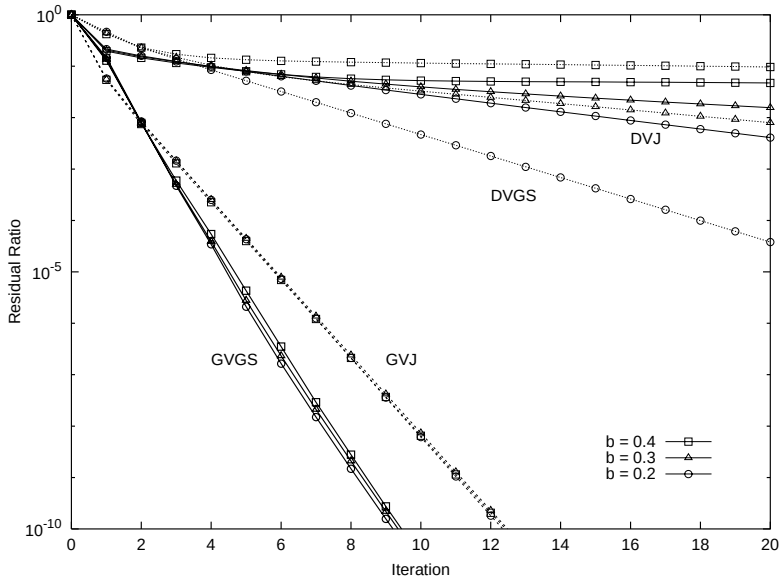

FIGURE 6 Woo-Sun Yang & J. R. Baumgardner

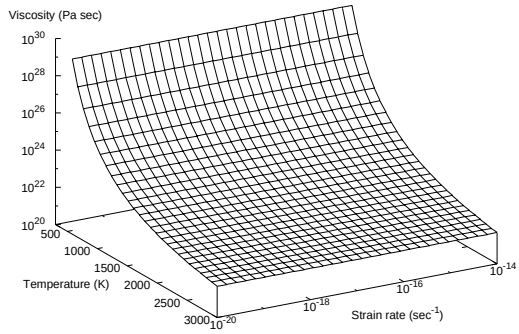

(a)

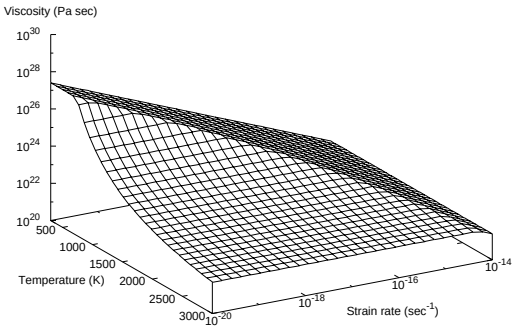

(b)

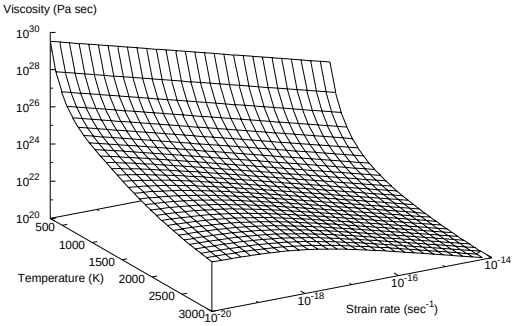

(c)

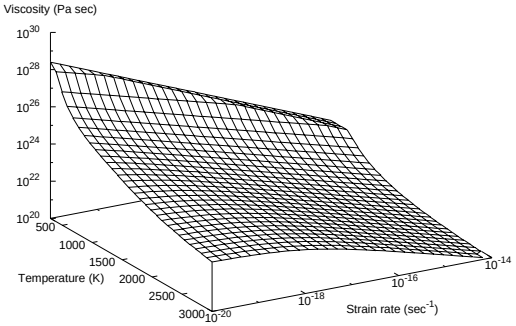

(d)

FIGURE 7 Woo-Sun Yang & J. R. Baumgardner

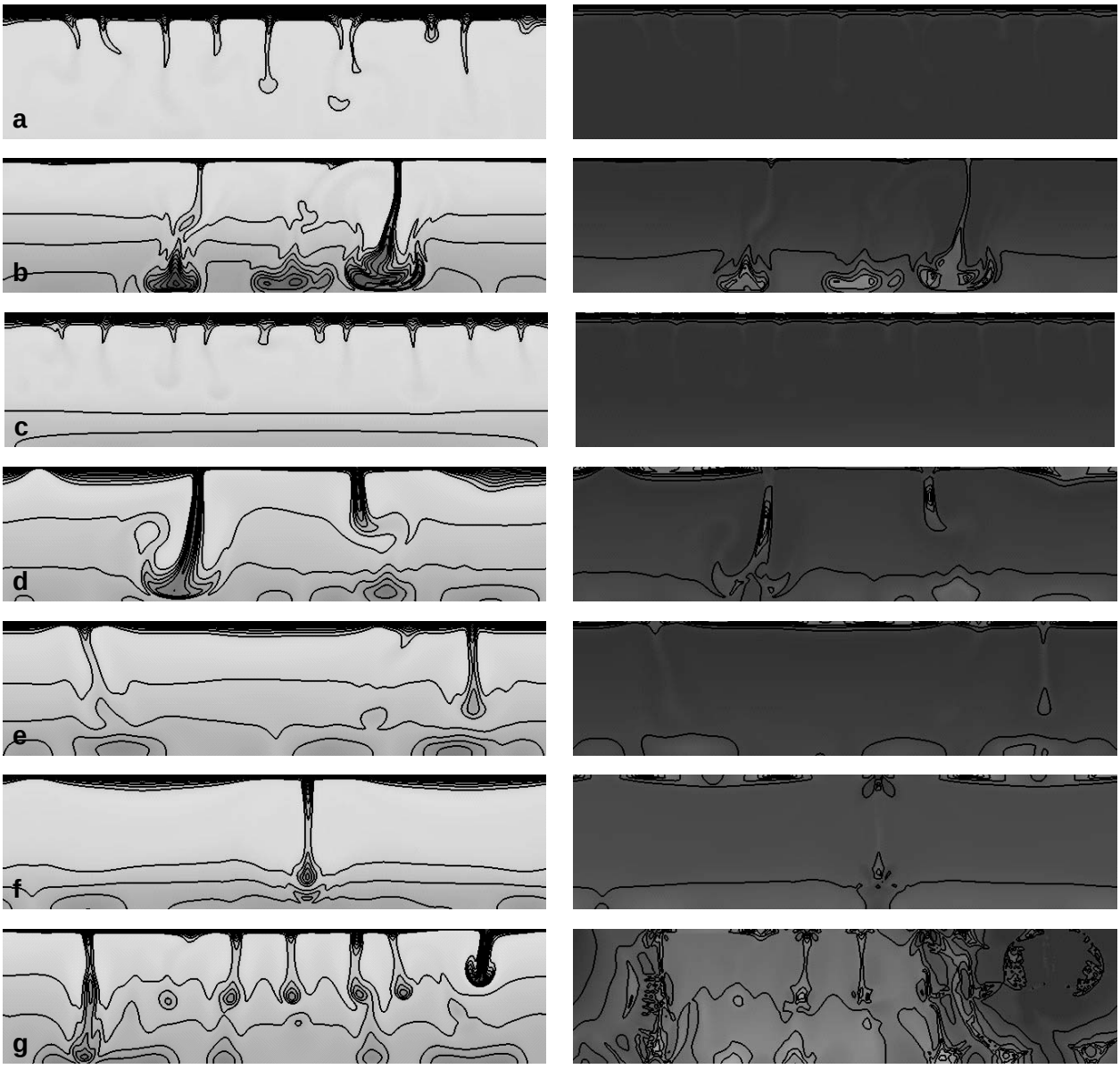

FIGURE 8 Woo-Sun Yang & J. R. Baumgardner

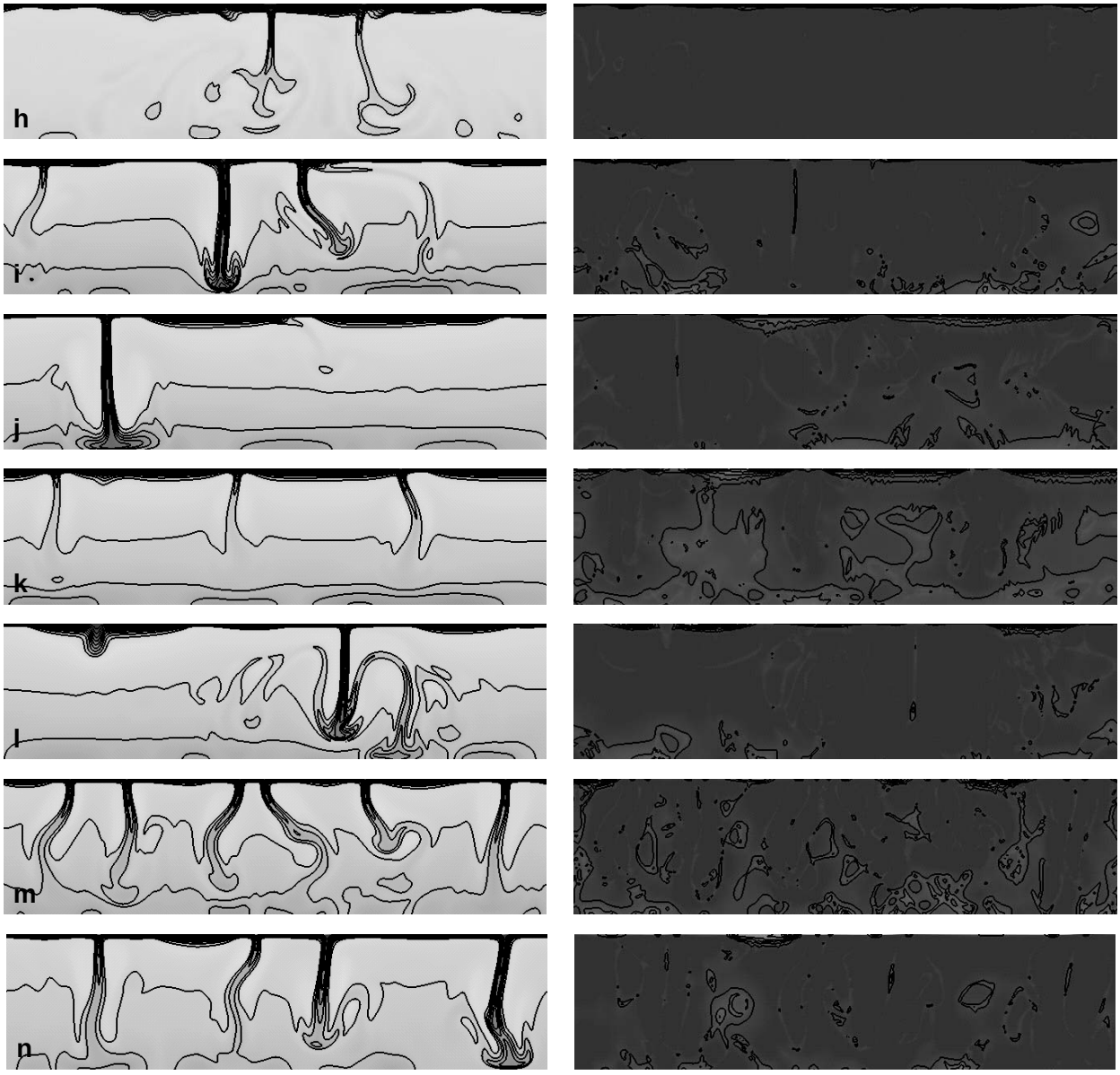

FIGURE 8 Woo-Sun Yang & J. R. Baumgardner

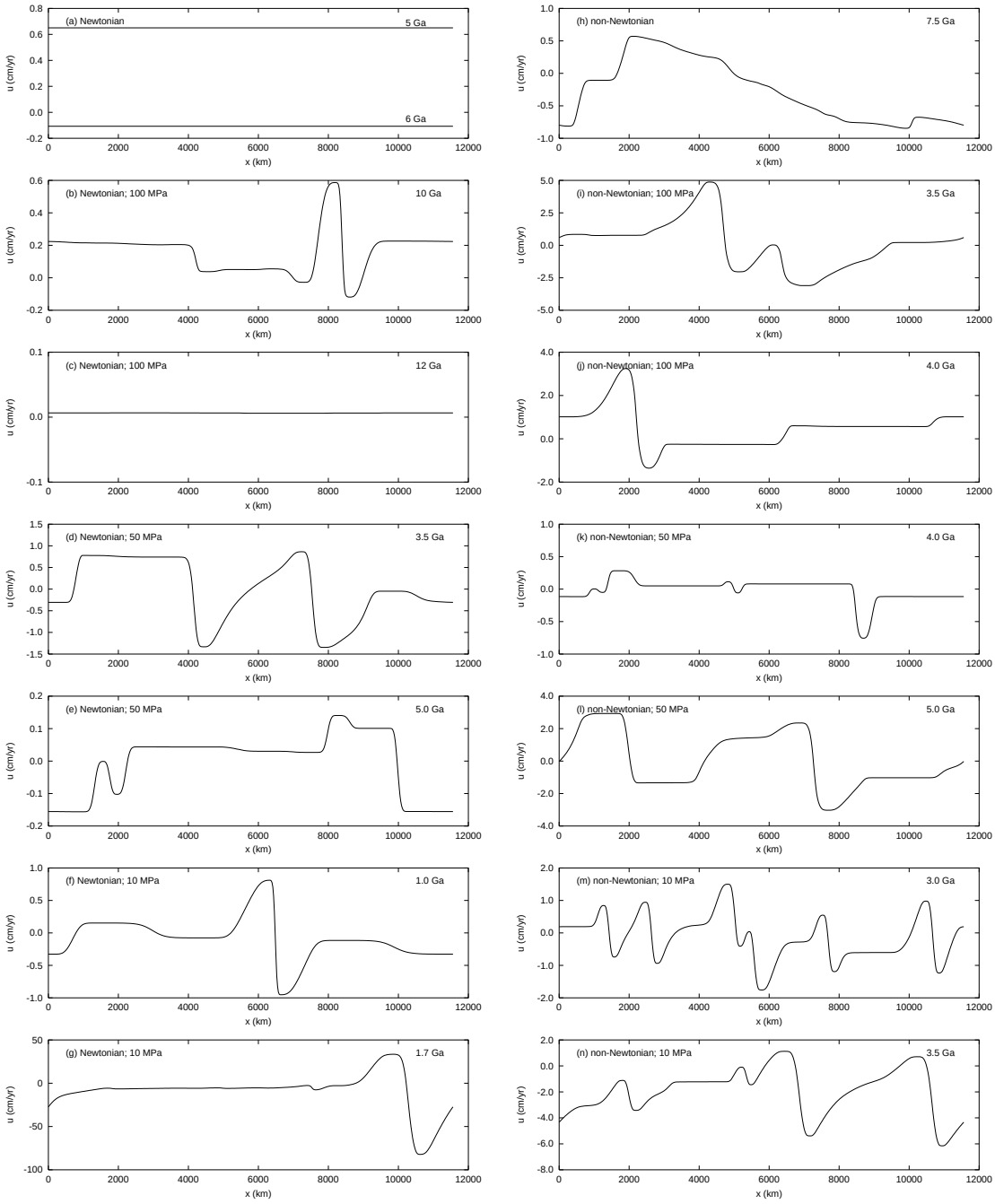

FIGURE 9 Woo-Sun Yang & J. R. Baumgardner

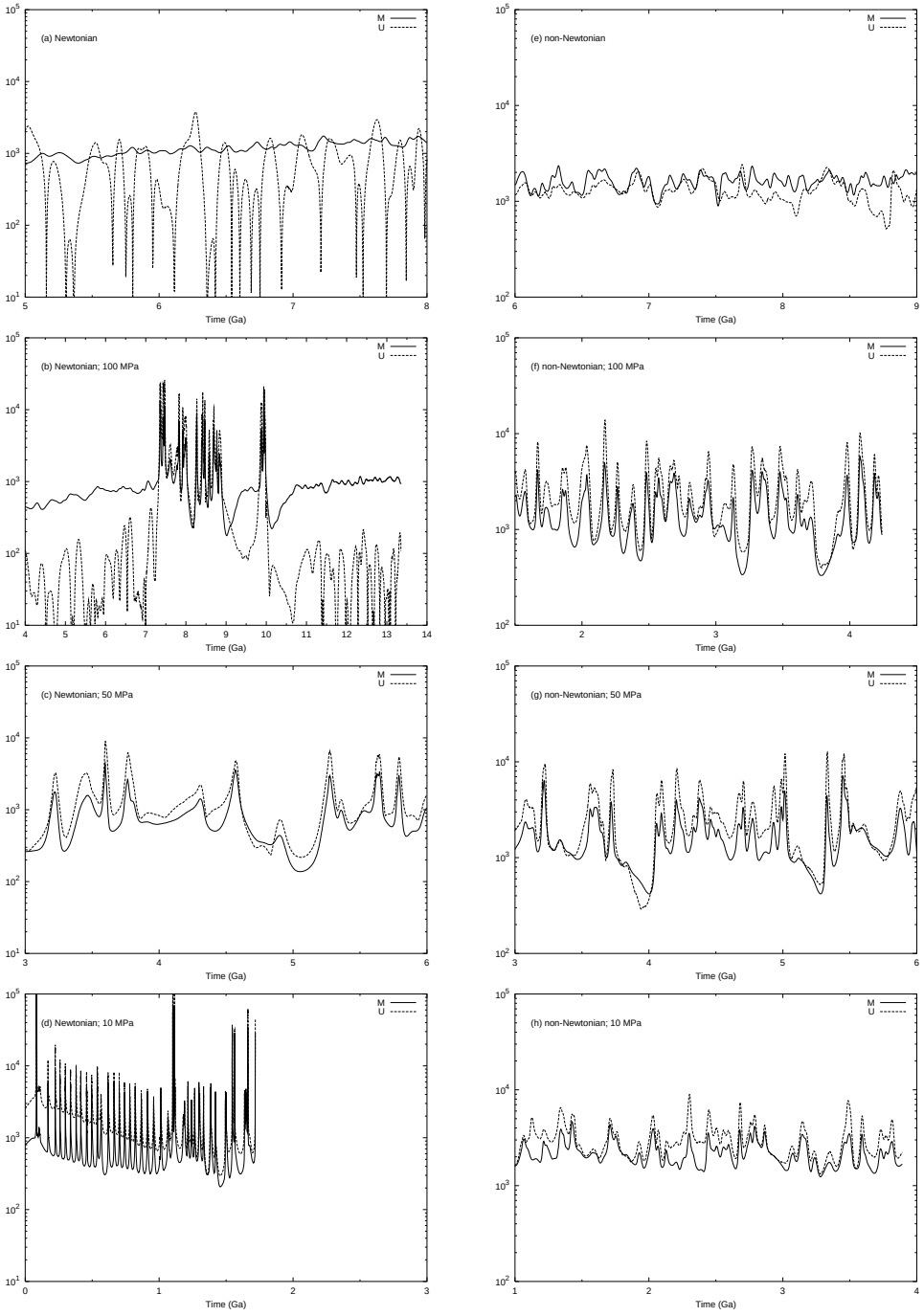

FIGURE 10 Woo-Sun Yang & J. R. Baumgardner

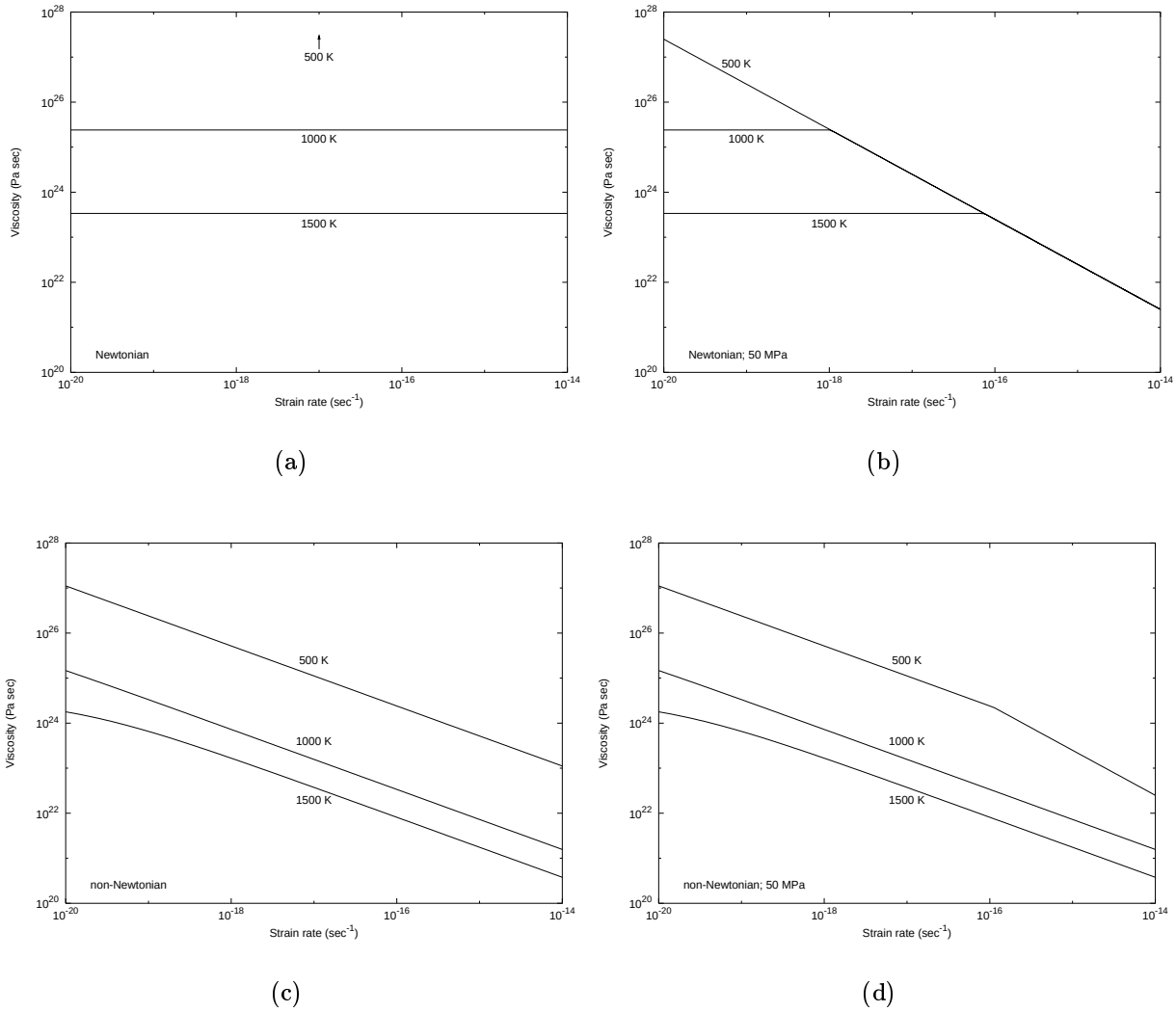

FIGURE 11 Woo-Sun Yang & J. R. Baumgardner